Chapter 20

Stimulated Raman scattering imaging with small vibrational probes

Haomin Wang, Jiajun Du, Dongkwan Lee, and Lu Wei
California Institute of Technology, Pasadena, CA, United States

20.1 Introduction

Small molecules with the size on the order of approximate 1 nm (Fig. 20.1A) play crucial roles by participating in and regulating a broad spectrum of biological and pharmacological processes. Small molecules function at different length scales in biological systems, ranging from the molecular level (~1 nm), the subcellular level (0.1–10 μm), the cellular level (10–100 μm), to the tissue level (>100 μm) [1]. The complex hierarchical organization of biological systems is by no means homogeneous, with numerous small molecules and biomacromolecules coexisting and cofunctioning toward the manifestation of biological activities (Fig. 20.1A). For example, at the subcellular level, functional proteins are synthesized from small-molecule building blocks of amino acids through transcription and translation [2]. At the tissue level, small-molecule hormones are used for intercellular signaling between tissues [3]. Knowledge of how small molecules transform physically and chemically within biological systems is necessary to get a comprehensive picture of how life behaves.

To obtain spatiotemporal information of small molecules involved in processes in living systems, fluorescence microscopy is usually the method of choice for its desired selectivity, sensitivity, and spatial resolution. However, there are intrinsic limitations for fluorescence microscopy in imaging small molecules. Most functional small molecules, such as nucleotides, amino acids, fatty acids, choline, glucose, and drugs, are naturally nonfluorescent. To image them via fluorescence, fluorophores must be used as labels. Because the introduced fluorophores are usually bulkier than the small molecule targets (Fig. 20.1A), they are likely to alter the physicochemical properties of labeled small molecules with respect to distribution, interaction, and dynamics. For instance, the intrinsic structure and composition of lipid rafts can be changed by tagged fluorescent probes [4]. Nile red, a staining dye used in fluorescence microscopy to label lipid droplets, has been shown to nonspecifically label other cellular structures as well [5, 6]. Therefore, a different contrast mechanism with the requirement of less perturbative probes is more desired for imaging small biomolecules.

Stimulated Raman scattering (SRS) microscopy presents an alternative contrast mechanism to map the distribution of small molecules through the vibrational excitation of chemical bonds [7–10]. With the stimulated emission quantum amplification and under the tight focus approximation, SRS can boost the cross section of spontaneous Raman by a factor of 10^8 and reach shot-noise limited signal-to-noise ratio with the radio-frequency (RF) modulation-transfer scheme [11–13]. Compared to another well-established coherent Raman scattering technique, coherent anti-Stokes scattering (CARS), SRS signals are free from nonresonant background and proportional to the concentrations of the analytes, which enables straightforward interpretations of chemical mapping to generate concentration maps [14]. Similar to two-photon fluorescence microscopy [11], SRS microscopy adopts spatiotemporally synchronized near-infrared pump and Stokes beams. This two-laser scheme permits SRS with background-free imaging in aqueous environments, diffraction-limited spatial resolution of a few hundreds of nm [15], and 3D optical sectioning capability into cells and tissues [16]. Label-free SRS imaging has been demonstrated for living microalgae, skins, and tissues of live animals with a video-rate of 25–110 frames per second [17–19], which is essential for deciphering various types of kinetics in cell biology [20].

By exploiting intrinsic Raman spectra of biomolecules, label-free SRS microscopy with chemical-bond specificity has been routinely utilized to map a series of metabolites and drugs, revealing their spatial distributions in live cells and tissues and enabling molecule-based diagnosis [1, 12, 13, 15, 21, 22]. In label-free SRS microscopy, targeted chemical bonds such as O—H, C—H, C═C, C═O, S═O, and O—P—O usually fall into the cell fingerprint region (600–1800 cm^{-1}, Fig. 20.1B), where the imaging specificity is often compromised because many biomolecular species share the same or overlapped Raman signatures [23]. Besides, Raman cross sections of these chemical bonds in the fingerprint region are also limited, restricting the SRS detection sensitivity to the millimolar level [11]. This limitation renders many biomolecules with lower

Stimulated Raman Scattering Microscopy. https://doi.org/10.1016/B978-0-323-85158-9.00023-3
Copyright © 2022 Elsevier Inc. All rights reserved.

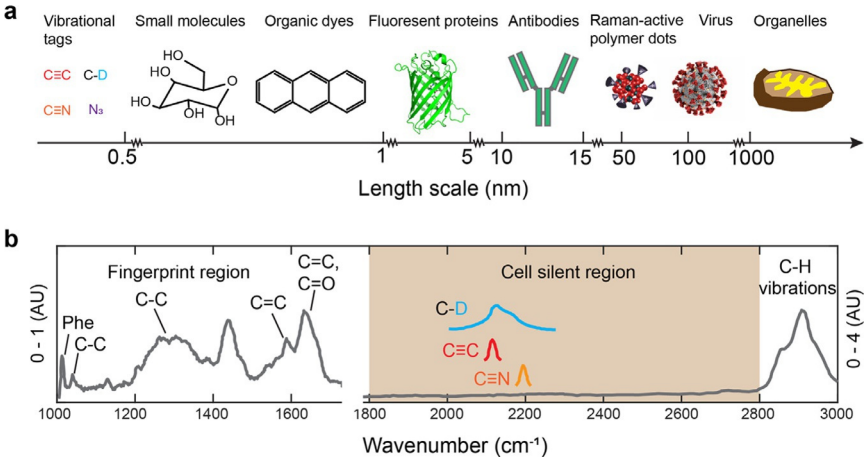

FIG. 20.1 Relevant size chart of biological systems and Raman spectra of cells. (A) Size comparisons for a series of Raman probes, fluorescent probes, biological species, and biostructures across the length scales. (B) A typical Raman spectrum of mammalian cells. There are no Raman peaks of endogenous species within the cell silent region, while Raman peaks of introduced vibrational probes such as C—D, C≡C, and C≡N could be utilized to report cell activities without background. *(Panels A and B: Adapted from F. Hu, L. Shi, W. Min, Biological imaging of chemical bonds by stimulated Raman scattering microscopy. Nat. Methods 16 (2019) 830–842).*

concentrations undetectable. Moreover, the performance of label-free SRS imaging in capturing dynamic metabolisms such as turnover of amino acids and lipids is less satisfying, because only the steady-state distribution of biomolecules is mapped. To further push the boundaries of SRS applications, nonperturbative vibrational imaging probes can be utilized to achieve higher sensitivity and selectivity, as well as the ability to report chemical regulations in many specific biological pathways. Hence, a combination of SRS microscopy with strong and selective Raman-active vibrational probes is much needed to track the spatiotemporal distribution of molecules of interest in biological systems with high sensitivity and molecular specificity.

The development and applications of vibrational probes have been indeed expanding greatly in both spontaneous Raman and SRS spectroscopy and microscopy. Shen et al. have reviewed a range of vibrational probes, including the triple bonds and isotopes, for their targeted molecules, spectral contrasts, and common applications [1]. Yamakoshi et al. have also summarized relative Raman cross sections of a series of vibrational probes [24]. With the addition of a few atoms or the exchange to isotopes, Raman tags can add distinctive and strong Raman signatures within the cell silent window (Fig. 20.1B) into the molecules of interest, which allows for rapid Raman imaging with high detection specificity and sensitivity. Compared with fluorescent proteins and organic dyes, Raman vibrational probes are much smaller in size as they only possess simple chemical bonds instead of whole molecules, thus preserving most of the native properties of targeted molecules when installed as imaging tags. This minimal labeling strategy is especially desired for labeling small molecular metabolites, such as nucleosides, amino acids, and glucose. Particularly, the tagged chemical bonds of alkynes with specific Raman signatures are also the most popular targets in bioorthogonal chemistry using click chemistry [25–27]. With such advantages, SRS imaging of small vibrational probes has opened new doors for bioorthogonal chemical imaging [16], yielding a series of insightful discoveries in de novo biosynthesis, cell and tissue metabolism, pharmaceutical applications, and chemical sensing [1, 12, 13, 15, 16, 21, 28, 29]. In the following sections, we will first give an overview of the principle and design of different categories of vibrational probes. Then, we will review and discuss representative SRS imaging applications with these vibrational probes across various areas of biology in live cells and tissues.

20.2 Principle

20.2.1 Triple-bond vibrational probes

Going beyond the label-free imaging scheme from the fingerprint region, Raman scattering within the cell silent region (1800–2600 cm^{-1}, Fig. 20.1B) is most desirable for sensitive and specific imaging. Triple bonds, including alkyne (C≡C), nitrile (C≡N), isonitrile (N≡C), and their derivatives all have sharp and strong Raman peaks in the cell silent window. These triple bonds were first developed as reporters in spontaneous Raman microscopy and surface-enhanced Raman spectroscopy (SERS) [24, 30, 31]. Because triple bonds often come with large Raman cross sections, they are especially useful in imaging targeted biomolecules with lower abundances in live cells and tissues. For example, the detection limit of SRS for C≡C in alkyne-labeled thymidine analog 5-ethynyl-2′-deoxyuridine (EdU) could reach 200 μM with 100 μs acquisition time [32], which is significantly improved from the mM detection limit recorded with the label-free

SRS [8]. The small size of triple-bond groups also introduces few perturbations into the intrinsic properties of targeted molecules. A list of reported structures of tripe-bond tagged metabolites, drugs, chemical sensors, etc., is provided in Fig. 20.2.

The first demonstration of SRS imaging of alkyne-tagged small biomolecules traces back to 2014. Using alkyne-tagged small-molecule metabolic analogs (Fig. 20.2, Section I) to deoxyribonucleosides, ribonucleosides, amino acids, choline, and fatty acids, de novo biosynthesis of DNA, RNA, proteins, triglycerides, and phospholipids were visualized in live cells and animals [27, 32]. SRS imaging of alkyne-tagged mannose and glucose analogs was also reported shortly after, revealing the spatial distribution of glycan and heterogeneous glucose uptake activities in cells and tissues [33, 34]. Furthermore, three-color SRS imaging of DNA, RNA, and lipids in living mammalian cells was achieved by using ^{13}C-edited alkyne tags (Fig. 20.2, Section III) [35]. In addition to alkyne tags, nitrile and isonitrile groups also have strong and distinctive Raman peaks in the cell silent window. Small molecules and metabolites bearing nitrile and isonitrile groups have been visualized by SRS imaging, such as fungicide chlorothalonil in plant tissues [36] and pathogen-produced tyrosine derivative rhabduscin in bacteria (Fig. 20.2, Section IV) [37].

Multiple alkyne groups can also form a conjugation system to further enhance Raman signals for chemically modified metabolic analogs, while the trade-off between the SRS signal and probe size must be considered in the rational design of vibrational probes case by case. Phenyl-diyne tagged cholesterol (Fig. 20.2, Section I) has been adopted in assessing cholesterol storage in live cells and *C. elegans* by SRS imaging [38]. The intracellular distributions and pathways of synthesized diyne-bearing analog to ferrostatin (Fig. 20.2, Section IV), a small-molecule drug, could also be captured by SRS in live cells [39]. Meanwhile, narrowband Raman peaks of triple-bond conjugation systems can be tuned by changing localized polarizability in multiple ways, such as changing the length of the conjugation chain [38, 40–42], bond-selective isotope doping [41, 42], and end-capping substitution [41, 42]. Further conjugation beyond diyne may make the probes less suitable for tagging small metabolites, but more suited as direct imaging probes for organelles and protein targets. For example, polyyne scaffold can extend from diyne to 6-yne for multicolor bio-imaging. With rational chemical editing to fine-tune the narrow Raman peaks, this scaffold can compose a suitable tool kit for developing a series of optical-multiplexed vibrational probes. Notably, a palette of supermultiplexed Raman probes based on engineered polyyne, termed as carbon rainbow or Carbow (Fig. 20.2, Section VI), was developed and reported to deliver 20 resolvable colors and barcoding capabilities in the cell silent region via SRS imaging, in which Raman signals increases exponentially with the number of conjugated triple bonds [42]. Another group of polydiacetylene-based ultra-strong vibrational topochemical polymers, named poly(deca-4,6-diynedioic acid) (PDDA, Fig. 20.2, Section VI), which holds up to $\sim 10^4$-fold signal enhancement compared to conventional alkynes, has also been developed recently [43]. The side chain of such polydiacetylene-based probes can be modified to target specific organelles in cells, enabling subcellular specificity. Recently, Wei et al. have developed a series of electronic preresonance enhanced Manhattan Raman Scattering (MARS, Fig. 20.2, Section VI) dyes based on engineering near-infrared-absorbing xanthene backbones [41], delivering 20 distinctive Raman colors. A more detailed review of MARS dyes will be covered in Chapter 21.

20.2.2 Isotope-based vibrational probes

Assuming the harmonic oscillation, the vibrational frequency of a chemical bond is inversely proportional to the square root of its reduced mass. Thus, Raman peak positions can be modulated by using stable isotope labeling. The most representative stable isotope used in Raman spectroscopy is deuterium (D). Replacing C—H with C—D increases the reduced mass of the oscillator, which in turn redshifts the Raman peak of C—H stretch from 2900 to 2100 cm^{-1} of C—D, which falls into the desired cell silent window. In contrast to small alkyne tags, stable isotopes introduce even fewer perturbations into targeted molecules. Isotope-substituted biomolecules often hold extremely similar biophysical and biochemical properties to their unsubstituted counterparts (e.g., deuterium to hydrogen). Such minimal labeling is essential for certain targets as in some cases that alkyne-labeled small vibrational probes do not fully resemble their natural counterparts in biological systems. For example, although homopropargylglycine (Hpg) has been demonstrated as a successful alkyne-labeled analog of methionine (Met) that could be recognized by the natural tRNA synthetase [44], it has also been found to show a 500 times slower cell incorporation rate than Met [45]. Moreover, alkyne-labeled vibrational probes usually require custom synthesis, while most stable-isotope labeling can be carried out using commercially available resources. Although Raman signals of stable isotope-labeled chemical bonds are weaker than alkyne bonds (Raman peak intensity of a C—D bond is about 30–40 times weaker than a single alkyne) [24, 32], due to the enormous amount of stable C—H groups in biomolecules, the high concentration of stable C—D groups after isotope labeling still provides adequate detection sensitivity for SRS microscopy.

In this regard, proteins with high concentrations of C—H groups (up to a few molar considering an average cellular protein concentration of about 2 mM) [46] are ideal to be deuterated and detected by SRS. The de novo biosynthesis of proteins, which is closely related to complex behaviors of cells, such as cell proliferation and response to stimuli, is

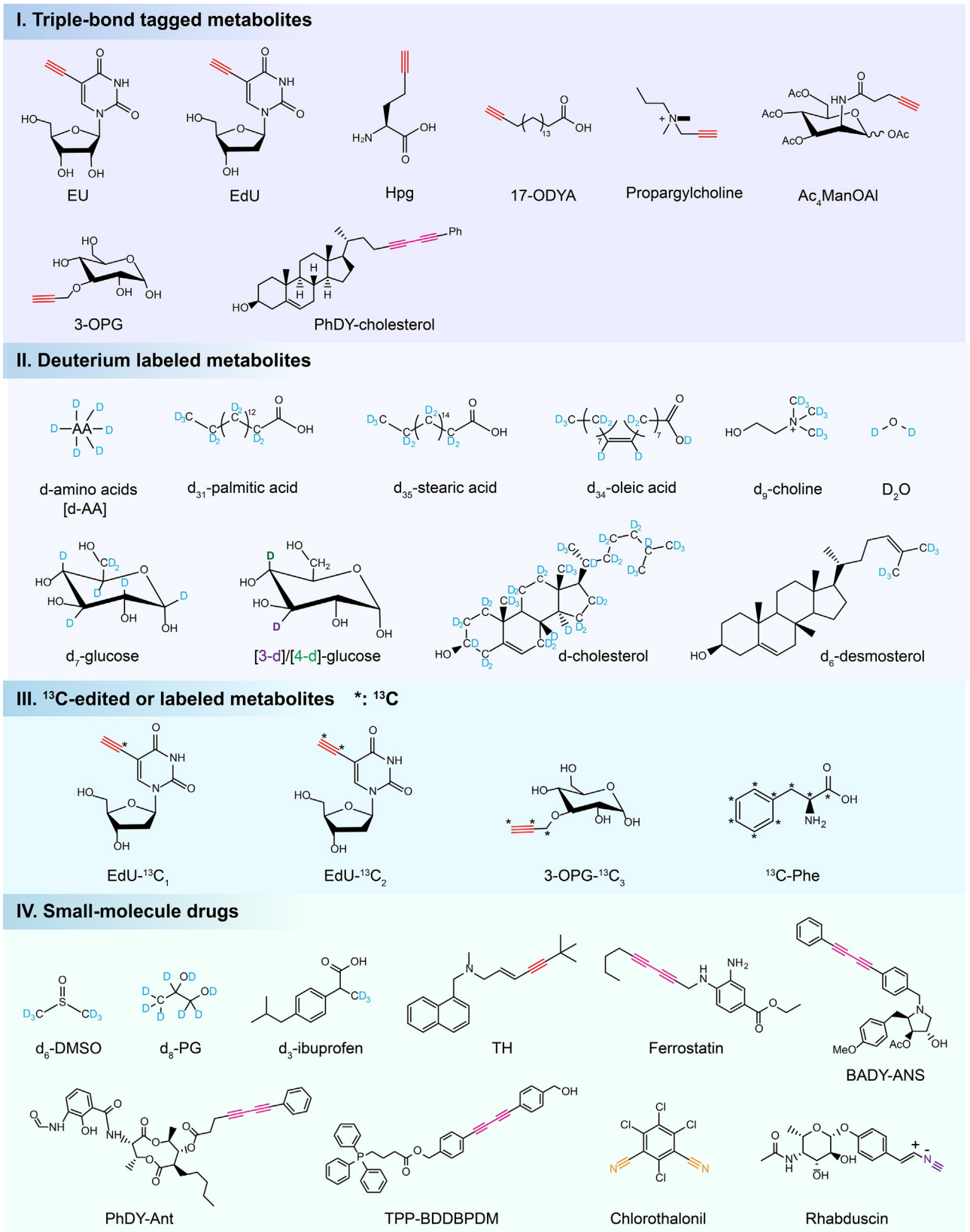

FIG. 20.2, CONT'D

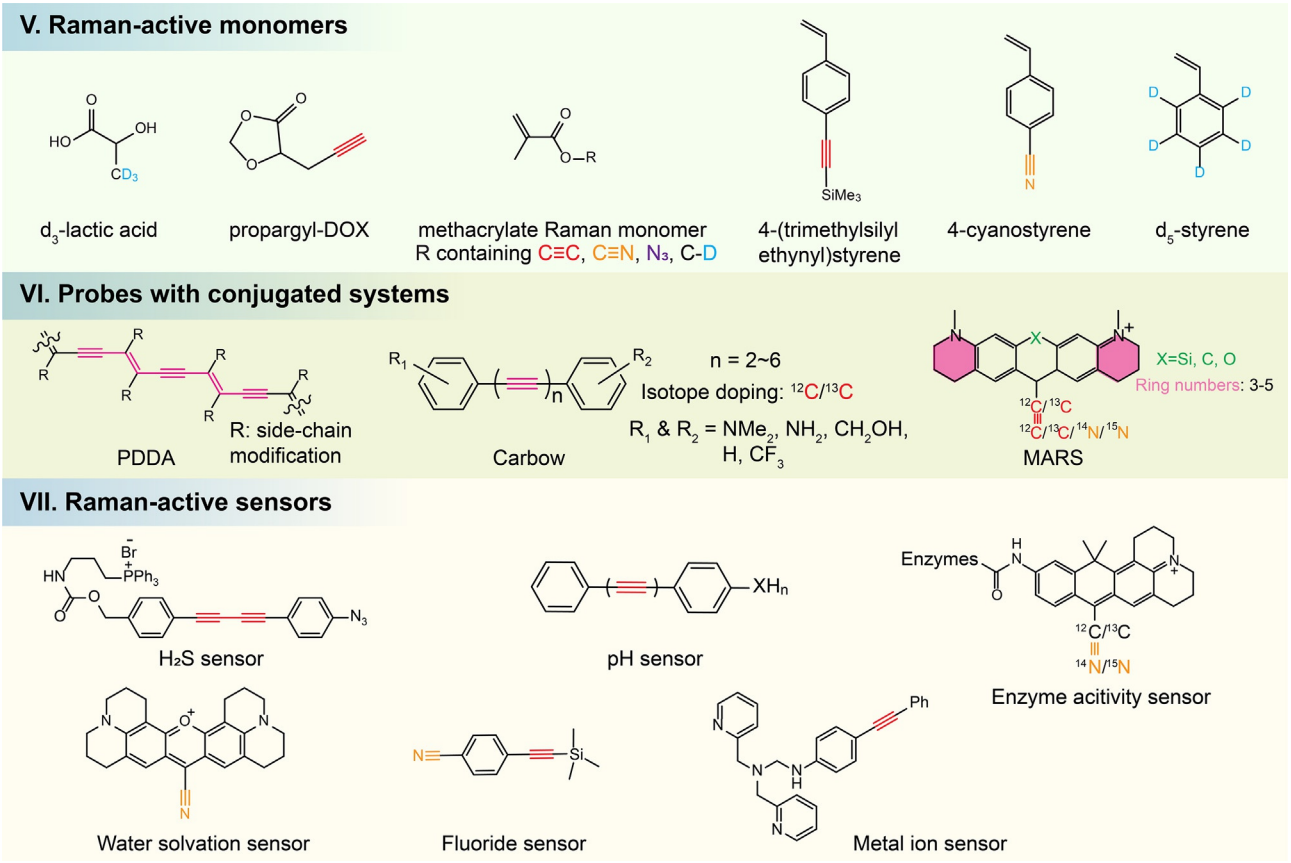

FIG. 20.2, CONT'D A list of reported chemical structures for vibrational probes across various categories for SRS microscopy. *EU*, 5-ethynyl uridine; *EdU*, 5-ethynyl-2′-deoxyuridine; *Hpg*, homopropargylglycine; 17-*ODYA*, 17-octadecynoic acid; *Ac4ManOAl*, peracetylated N-(4-pentynoyl)mannosamine; 3-*OPG*, 3-*O*-propargyl glucose; *Phe*, phenylalanine; *PG*, propylene glycol; *TH*, terbinafine hydrochloride; *BADY-ANS*, N-4-(4-phenyl-1,3-butadiyn-1-yl)benzyl anisomycin; *PhDY-Ant*, phenyl-diyne antimycin; *TPP*, triphenylphosphonium; *BDDBPDM*, (buta-1,3-diyne-1,4-diylbis (4,1-phenylene)dimethanol; *DOX*, 1,3-dioxolan-4-ones; *PDDA*, poly(deca-4,6-diynedioic acid); *MARS*, Manhattan Raman Scattering.

the last step of the central dogma [47]. To gain insights into this process, a series of deuterated amino acids (d-AAs, Fig. 20.2, Section II) has been developed and metabolically incorporated into cells to mimic the biosynthesis of proteins. SRS imaging of newly synthesized proteins enriched in live neurons, brain slices, and animals has been achieved through the detection of C—D vibrations, while unincorporated d-AAs are too dilute to be detected [48]. Beyond protein synthesis, complex protein metabolism including degradation could also be traced with pulse-chase analysis with *d*-AAs. Moreover, the large amount of C—D bonds after the *d*-AA incorporation has enabled fast volumetric SRS mapping of proteins in a large 12 mm^2 brain tissue in a short time of 2.2 min [14].

In addition to amino acids, a great wealth of other biomolecules with replaceable C—H bonds also exist in biological systems. Deuterated small molecules (Fig. 20.2, Section II) have been adopted to investigate a wide range of corresponding biomolecular species, including choline [49], fatty acids [50], sterols [51], glucose [52], and drugs [53]. For example, by utilizing distinctive Raman spectral features of C—D bonds in different chemical species, in situ metabolisms of proteins, lipids, and DNA in cells, tissues, and animals have been visualized by deuterium oxide (D_2O) probing with SRS (DO-SRS), which employs heavy water as a universal labeling agent [54]. Additionally, the downstream metabolic products of glucose can also be imaged and traced by tracking the turnover of d_7-glucose in live cells and animals using a methodology named spectral tracing of deuterium isotopes (STRIDE) SRS [55].

Besides the commonly used deuterium labels, ^{13}C labeling on carbon bonds (Fig. 20.2, Section III) could also shift their vibrational frequencies and achieve bioorthogonal SRS imaging. In a proteome degradation study, the ring-breathing mode of ^{13}C-phenylalanine (^{13}C-Phe) at 968 cm^{-1} was used as an indicator for mapping the concentration of newly synthesized proteins, while the same mode of ^{12}C-Phe at 1004 cm^{-1} was used for imaging preexisting proteins [56]. The proteome degradation of old proteins in live cells was clearly visualized as a function of time by mapping the SRS intensity ratio

of $^{12}C/(^{12}C+^{13}C)$. Another application of ^{13}C labeling made use of ^{13}C-edited alkynes for 3-*O*-propargyl-D-glucose (3-OPG-$^{13}C_3$) to enable two-color SRS imaging of glucose uptake and metabolism in cell transitions and brain tissues when combined with d_7-glucose [57]. The ratiometric images based on C-D/$^{13}C\equiv{}^{13}C$ vibrational contrast revealed a clear difference in glucose metabolism between normal and cancer cells. As mentioned in the previous alkyne section, ^{13}C-labeled alkyne probes have also enabled multicolor SRS imaging of DNA, RNA, and lipids in living cells [35].

20.2.3 Raman-active monomers for nanoparticles

Nanoparticles are valued as an enrichment scaffold to amplify the otherwise weak Raman signals. To obtain better sensitivity and specificity, the idea of vibrational probes has also been incorporated into the synthesis of Raman-active nanomaterials. With the advantages of biocompatibility and easily tunable scaffold, nanoparticles bearing vibrational probes are readily applicable in disease diagnosis [58], drug delivery [59, 60], and cell sorting applications [61]. Several reported Raman-active monomers for polymerized nanoparticles are listed in the Section V of Fig. 20.2.

One example of nanoparticles used with SRS microscopy is Raman-active polymer dots. The uptake of alkyne, nitrile, and deuterium-tagged polymer dots were imaged by SRS with three distinctive colors [61]. These Raman-active polymer dots exhibit low cytotoxicity, high photostability, and the potential to sort different phenotypes of cells. Additionally, a library of Raman-active poly(methacrylate) (PMA) beads bearing alkyne, nitrile, azide, and deuterium has been developed and used as multicolor SRS probes in imaging tumor cells and tissues in vivo [58]. Furthermore, SRS imaging of the nanoparticle distribution in brain tissues has been demonstrated with alkyne-tagged nanoparticles of biocompatible poly(lactic acid-*co*-glycolic acid) (PLGA), revealing the potential of PLGA nanoparticles in delivering drugs selectively to microglia [59]. Polymerized nanoparticles can serve as carriers for small Raman probes as well. The incorporation of Carbow probes onto polystyrene beads could enable supermultiplexed barcoding (theoretically up to ~60,000 barcodes) in cell labeling with little spectral cross talk [42]. With high sensitivity, spectral tunability, and improved biocompatibility, Raman-active nanoparticles can assist in high-throughput screening and pharmaceutical studies.

20.2.4 Raman-active targeted probes and chemical sensors

Subcellular organelles and specific proteins can also be imaged by SRS microscopy through tailoring the structure of vibrational probes with targeting moieties, high sensitivity, and suitable membrane permeability. For example, functionalized Carbow probes (i.e., the conjugated alkynes) could specifically label mitochondria, lysosome, plasma membrane, endoplasmic reticulum, fatty acids, and structural proteins [42]. Similarly, by changing the side groups of PDDA from amine to targeting peptides, three PDDA derivatives were developed for targeted imaging of lysosome, mitochondria, and nucleus [43].

Chemical sensing is also achievable through the use of target-specific Raman vibrational probes. Generally, Raman sensors can specifically bind to or react with molecules of interest. The resulting bound or chemically converted sensor structures hold a shifted Raman peak than that of the original sensor molecules. For chemical sensing in living systems, vibrational probes should be not only highly sensitive and specific, but also photostable and biocompatible. To this end, a series of Raman-active chemical sensors (Fig. 20.2, Section VII) has been developed and demonstrated for various purposes, including for sensing hydrogen sulfide (H_2S) [62], pH [63], fluoride ions [64], metal ions [65], enzyme activities [66], and water solvation states [67], most of which have been demonstrated in living cells. More detailed descriptions of each application will be covered in the following section.

20.3 Applications

20.3.1 Small vibrational probes in metabolisms

Small-molecule vibrational probes act as chemical reporters for a broad spectrum of biological studies [68], where deep insights into biosynthesis and metabolism can be obtained by tracking the penetration, uptake, transportation, distribution, and conversion of the molecules with small vibrational probes at different spatiotemporal stages. With the expanding library of Raman vibrational probes, biosynthesis and metabolism of nucleic acids, proteins, lipids, and glucose have been visualized by SRS microscopy with high sensitivity and subcellular resolution in live biological systems. In the following sections, we review some representative works to date in revealing biosynthesis and metabolism with vibrational probes using SRS microscopy.

20.3.1.1 Nucleic acid synthesis and turnover

Traditionally, nucleic acids are visualized by DAPI or Hoechst stain [69]. To examine the synthesis of DNA, nucleoside analogs such as bromodeoxyuridine (BrdU) could be used [70]. However, BrdU detection requires immunostaining under harsh staining conditions, which does not work with live cell measurements. Later, alkyne-bearing 5-ethynyl deoxyuridine (EdU) and 5-ethynyl uridine (EU) were introduced for monitoring DNA and RNA synthesis with bioorthogonal chemistry [71]. Nevertheless, to detect the incorporation of either EdU or EU, fluorescent labels with azides and click chemistry reaction are required, in which the copper complexes may induce unwanted cytotoxicity and disrupt normal cellular metabolism [72]. These limitations can be overcome by vibrational imaging. Label-free SRS imaging of total DNA has already been achieved in vivo [73]. Beyond the label-free scheme, SRS imaging coupled with alkyne-labeled nucleoside analogs can readily visualize and monitor the synthesis and turnover of nucleic acids in live cells and tissues. Such direct visualization of alkyne vibrations by SRS bypasses the complications from chemical modifications such as in click chemistry.

In 2014, alkyne-labeled EdU was first utilized in SRS imaging of newly synthesized DNA in living cells independently by Wei et al. [32] and Hong et al. [33]. Using SRS imaging of EdU-labeled DNA, the dynamic process of cell division of HeLa cells (Fig. 20.3A) and proliferation in *Caenorhabditis elegans* (*C. elegans*) germline was successfully resolved. In live mammalian hippocampal tissues, Hu et al. employed isotope-edited EdU labeling and found different DNA incorporation patterns through pulse-chase analysis, which is likely caused by two consecutive cell division cycles (Fig. 20.3B) [74]. Similarly, RNA turnover was monitored by incorporating alkyne-tagged EU into cells. With pulse-chase labeling, a much faster turnover of RNA (compared to DNA) with a short lifetime of $\sim$3 h was discovered in live HeLa cells (Fig. 20.3C) [32]. Furthermore, with isotope-edited EdU, EU, and alkyne-labeled 17-octadecynoic acid (17-ODYA), three-color SRS imaging of DNA, RNA, and lipids was demonstrated (Fig. 20.3D) [35], allowing for the unambiguous differentiation among three species in multiplex cell environments. SRS microscopy of alkynes hence allows direct bioorthogonal chemical imaging [16] on a wide range of labeled small-metabolites.

20.3.1.2 Protein metabolism

The symmetric vibration of CH_3 at 2940 cm^{-1} and amide I band centering around 1660 cm^{-1} are commonly used in label-free SRS microscopy to map the distribution of endogenous proteins [17, 19]. For example, similar to the traditional hematoxylin and eosin (H&E) staining, brain tumor boundaries and penetration fronts were delineated with stimulated Raman histology based on detecting C—H vibrations of proteins and lipids [76–78]. Misfolded amyloid plagues formed in Alzheimer's disease were identified spectroscopically with a small Raman peak shift of $\sim$10 cm^{-1} within amide I band, which was captured by label-free SRS [79]. However, label-free SRS imaging only maps the steady-state image of protein distributions. Dynamically monitoring the synthesis and turnover of proteome or specific proteins of interest with precise temporal information and fine chemical specificity would offer deeper understandings of metabolic dynamics in health (e.g., long-term memory formation) [80] and disease (e.g., cancer and neurodegenerative diseases) related bioactivities. Adoption of vibrational probe labeling could help achieve this goal.

Alkyne and isotope-labeled amino acids can be applied to tracing de novo protein biosynthesis and metabolism through SRS microscopy. As an example, alkyne-tagged Hpg was used as an analog to the natural Met to visualize protein synthesis, which revealed the spatial enrichment of newly synthesized proteins in the nucleoli (Fig. 20.3E) [32]. Also, as mentioned in the Principle section, ^{13}C-labeled phenylalanine (^{13}C-Phe) was applied with SRS imaging to quantify the degradation of cell proteome together with ^{12}C-Phe bearing endogenous proteins. With this strategy, the proteome degradation of cells transfected by neurodegenerative mutant huntingtin (mHtt) proteins were investigated by SRS imaging (Fig. 20.3F) [56]. The proteome degradation was found to be slower in cells with small polyglutamine (polyQ) inclusion bodies and normal in those with large polyQ inclusion bodies.

With deuterium labeling on the stable side chains, deuterated amino acids (*d*-AAs) allow metabolic labeling and bioorthogonal SRS imaging of protein synthesis through the cell's native translational machinery (Fig. 20.3G) [48]. High sensitivity and time-lapse SRS imaging of protein synthesis and degradation has been achieved in live HeLa cells, primary neuron cells, mouse brain tissues, and zebrafish in vivo, with superb biocompatibility from isotope labeling (Fig. 20.3G) [14, 48]. By rationally dividing *d*-AAs into two subsets based on their Raman signatures, Wei et al. also conducted two-color pulse-chase SRS imaging of mHtt proteins in live cells to reveal the dynamics of aggregate formation [14]. Recently, using deuterated glutamine (Gln-d_5) and hyperspectral SRS imaging, Miao et al. achieved specific and quantitative SRS imaging of polyQ aggregates. They managed to quantify aberrant mHtt proteins and normal cytosolic proteins sequestered to the same aggregates in live cells (Fig. 20.3H) [75, 81]. The SRS spectra of mHtt aggregations, cell backgrounds, lipid droplets, and nucleoli were also analyzed and compared (Fig. 20.3I), and a spectral dip at 2146 cm^{-1} was found to be indicative of the microenvironment, possibly the hydrogen bonding, of mHtt aggregates. In sum, amino acids labeled with

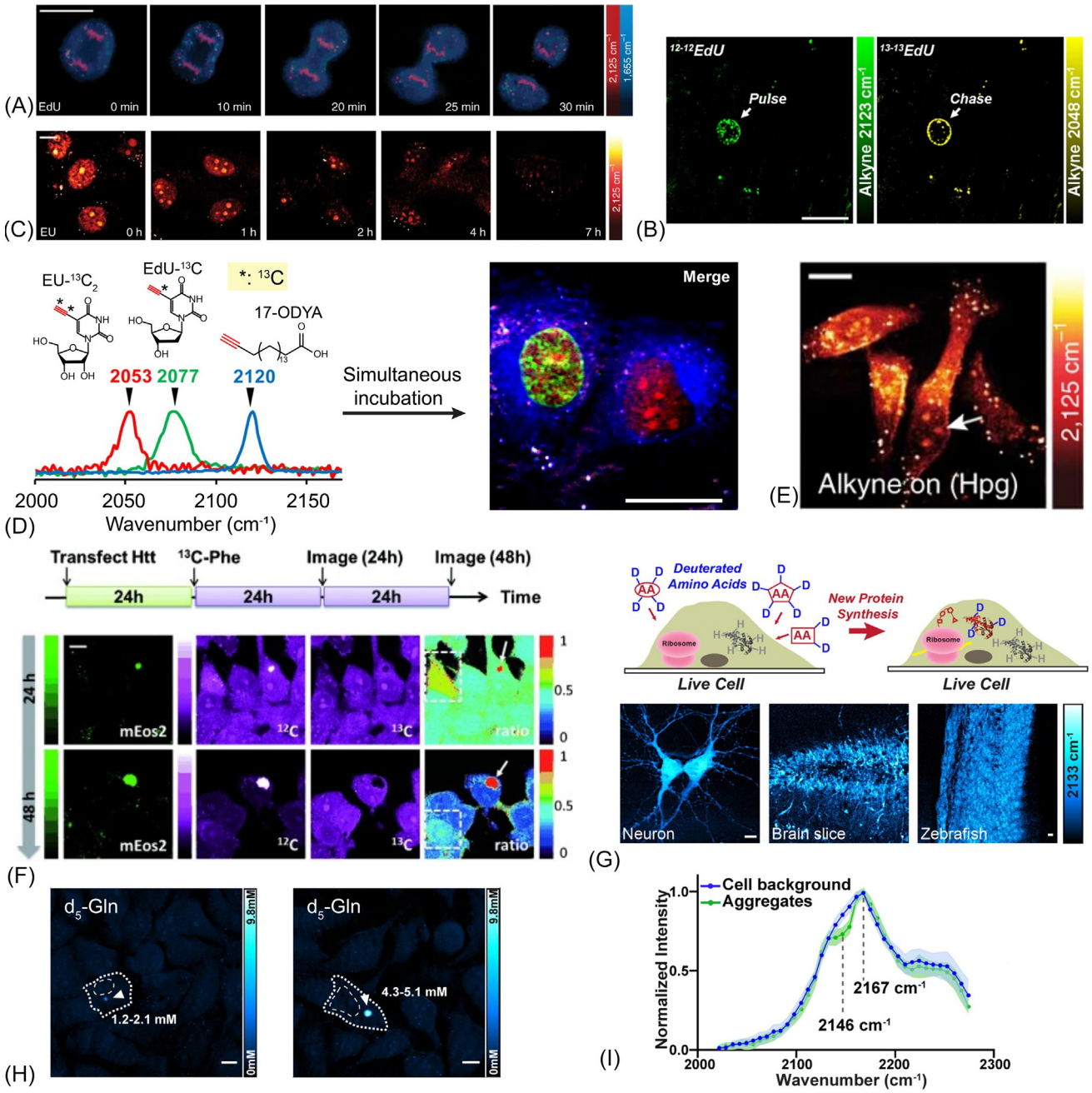

FIG. 20.3 SRS imaging of nucleic acids and protein metabolism. (A) Cell division tracking after incorporated with EdU for newly synthesized DNA. Scale bar: 10 μm [32]. (B) Two-color pulse-chase labeling of alkyne-tagged EdU isotopologues in rat hippocampal slices imaged by SRS microscopy. Different DNA incorporation patterns are observed. Scale bar: 20 μm [74]. (C) Decay of alkyne signals as a function of time is observed with SRS imaging following pulse labeling of EU in cells for probing RNA tournover. Scale bar: 10 μm [32]. (D) *Left*: Raman spectra of EU-$^{13}C_2$, EdU-^{13}C, and 17-ODYA. *Right*: Merged three-color SRS image of newly synthesized RNA, DNA, and fatty acyl derivatives in live HeLa cells treated simultaneously with EU-$^{13}C_2$, EdU-^{13}C, and 17-ODYA. Scale bar: 25 μm [35]. (E) SRS image of newly synthesized proteins after Hpg incorporation in live HeLa cells. Scale bar: 10 μm [32]. (F) Proteome degradation in HEK293T cells during Htt-Q94 aggregation with ^{13}C-Phe incubation (*top scheme*). *First column*: mEos2 fluorescence images, indicating the formation of inclusion body of polyQ. *Second and third columns*: SRS images of ^{12}C and ^{13}C channels. *Fourth channel*: $^{12}C/(^{12}C+^{13}C)$ ratio maps. Scale bar: 10 μm [56]. (G) *Upper*: a schematic illustrating the metabolic incorporation of d-AAs into cells' nascent proteins through natural cell machineries. *Lower*: SRS images of the C—D vibrational peak showing newly synthesized proteins in live neurons, brain slices, and zebra fish. Scale bars: 10 μm [48]. (H) SRS images of d_5-Gln-labeled mHtt-97Q aggregates. Quantifications of polyQ are shown on the images as local concentrations. Scale bars: 10 μm [75]. (I) Live-cell SRS C—D spectra of mHtt-97Q aggregates *(green)* and cell background *(blue)* [75].

vibrational probes have brought the protein metabolism study to a new level, where the de novo protein biosynthesis, intracellular protein dynamics, and protein dysfunctions can be captured and deduced unambiguously using bioorthogonal SRS microscopy.

20.3.1.3 Lipid metabolism

In the label-free SRS scheme, lipids are usually imaged and quantified by the strong C—H vibrations within 2800–3100 cm^{-1}, including CH_2 (around 2850 cm^{-1}) for total lipids and C═C—H bonds (3002–3015 cm^{-1}) for unsaturated lipids [82, 83, 89, 90]. Using these contrasts, distributions of triglycerides and cholesteryl esters in lipid droplets were imaged and quantified in cells and tissues (Fig. 20.4A) [82]. An increased amount of unsaturated lipids in ovarian cancer stem cells and spheroids was observed by Li et al. (Fig. 20.4B) [83], indicating that the lipid unsaturation level could be used as a metabolic marker for cancer cells. Other lipid species and related processes, including squalene (the cholesterol precursor, Fig. 20.4C) [84], cholesterol [91], and myelin degenerations [92] have also been found with deep implications in diseased states, such as cancer [76], cardiovascular diseases [93, 94] and amyotrophic lateral sclerosis (ALS) models [92]. Prominently, Yue et al. located the accumulation of cholesteryl ester in prostate cancer tissues and found the cancer proliferation and invasion could be impaired by the depletion of cholesteryl ester [95].

All above label-free investigations have laid the foundation for interrogating lipid accumulation and dynamics in a variety of diseases and underlined its significance. However, the C—H band within 2800–3100 cm^{-1} and the fingerprint region are congested with many different endogenous lipid species. To enhance the detection selectivity and monitor the dynamic turnover of specific lipids, small-molecule vibrational probes are attached to fatty acids and sterols, which makes it possible to specifically visualize the lipids of interest in the cell silent region. As an example, phenyl-diyne tagged cholesterol has been demonstrated as a close analog to natural cholesterol, providing ~88 times larger Raman signal than endogenous C═O mode and superb detection sensitivity of 31 μM [38]. The metabolism of phenyl-diyne-labeled cholesterol was investigated in a cellular model of Niemann-Pick type C disease, which showed that the cholesterol accumulates in lysosomes and relocates to lipid droplets after 2-hydroxypropyl-β-cyclodextrin treatment (Fig. 20.4D). Isotope-edited d_6-desmosterol, an intermediate species associated with cholesterol biosynthesis in the hepatitis C virus (HCV) replication, was adopted by Villareal et al. to study the desmosterol metabolism in HCV infected cells (Fig. 20.4E) [85]. The infection of HCV was shown to cause desmosterol to accumulate in viral NS5A protein-associated lipid droplets, suggesting the HCV replication may be directly affected by the desmosterol.

Background-free and quantitative SRS imaging of lipid synthesis and lipolysis of three different fatty acids in lipid droplets of *C. elegans* was performed by monitoring turnovers of alkyne-tagged 17-ODYA (Fig. 20.4F), deuterated palmitic acid (d_{31}-PA), and deuterated oleic acid (d_{34}-OA) [86]. Yu et al. used optical highlighter screening with subsequent d_{34}-OA labeling to track lipid synthesis and mobilization in the bone morphogenetic protein (BMP) signaling pathway mutants of *C. elegans* [96]. BMP mutants were found to express significantly accelerated lipid mobilization, while the lipid synthesis remains unaffected. With a similar strategy, d_{31}-PA was supplied to live hippocampal tissues, and uniform incorporation and metabolism of palmitic acid were found by SRS imaging of C—D bonds [74]. The endoplasmic reticulum (ER), the most abundant membrane system inside cells, was originally regarded as fluidic. However, with d_{31}-PA labeling, hyperspectral SRS microscopy revealed that the high concentration of saturated fatty acids perturbs ER membrane fluidity and induces the formation of phase-separated solid-like lipid domains (Fig. 20.4I), which cannot be solely visualized by fluorescence microscopy [87]. The minimally perturbative C—D labeling used in this study has opened doors for imaging spatiotemporal biophysics of cellular membrane with high resolution.

In addition to labeled fatty acids for imaging neutral lipids, other labeled metabolic precursors could be adopted to probe more aspects of lipid metabolism. Choline is an essential nutrient that mediates various membrane and bodily functions [97]. The newly synthesized choline phospholipids in live neurons could be visualized by SRS microscopy with the incorporation of alkyne-bearing propargylcholine (Fig. 20.4G) [32]. Hu et al. have also utilized deuterated choline (d_9-choline) to image free choline and choline-containing metabolites including phosphocholine, glycerophosphocholine, lipid-bound phosphatidylcholine, and sphingomyelin in living cells, neurons, and *C. elegans* [49]. Li et al. used isotope-labeled glucose (d_7-glucose) to study de novo lipogenesis of cancer cells through the tricarboxylic acid (TCA) cycle (Fig. 20.4H) [52]. The lipogenesis was found to be downregulated in prostate cancer cells in comparison to pancreatic cancer cells, indicating an altered fatty acid metabolism pathway may play a role in prostate cancer.

Working in conjunction with spontaneous Raman, lipidomics, and transcriptomics analysis, Du et al. have utilized SRS imaging of vibrational probes to achieve Raman-guided subcellular pharmaco-metabolomics [88]. Such an integrative subcellular omics strategy could help guide the deciphering of the metabolic controls across different cancer subphenotypes and is beyond what other common methods including mass spectrometry and fluorescence microscopy could achieve.

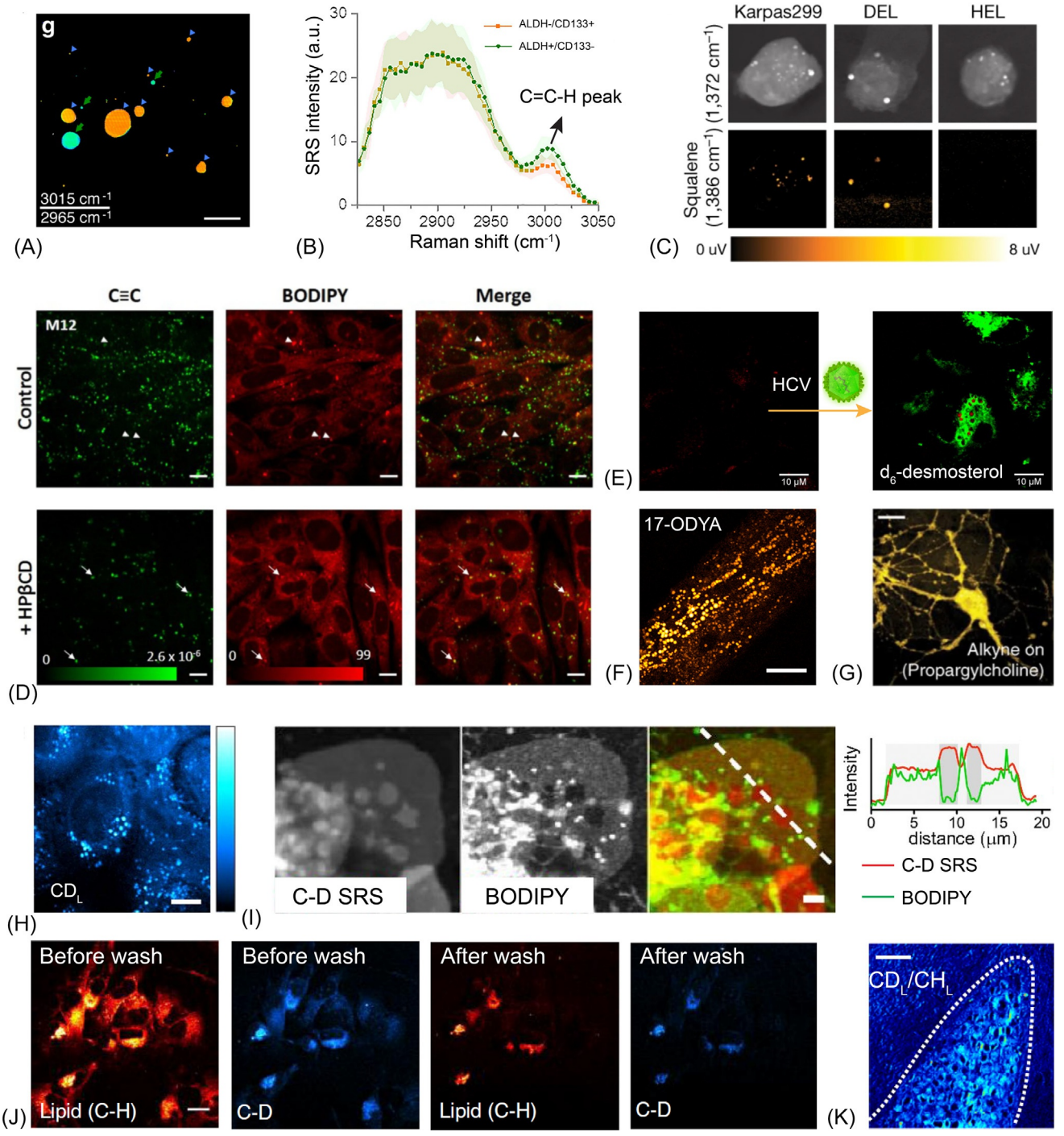

FIG. 20.4 SRS imaging of lipid metabolism. (A) A label-free ratiometric SRS image of triglycerides *(orange)* and cholesteryl esters *(green)* in lipid droplets. Scale bar: 20 μm [82]. (B) SRS spectra of lipid droplets in noncancer stem cells (ALDH−/CD133−) and cancer stem cells (ALDH+/CD133+). Increased unsaturated lipid level is a hallmark of cancer stem cells [83]. (C) SRS images of squalene accumulation in lipid droplets in anaplastic large cell lymphoma (ALCL) cells [84]. (D) SRS imaging of PhDY-cholesterol and two-photon-excited fluorescence imaging of BODIPY (stains lipid droplets) stained Niemann-Pick type C cells. After 2-hydroxypropyl-β-cyclodextrin (HPβCD) treatment, cholesterol relocates to lipid droplets. Scale bars: 20 μm [38]. (E) SRS images of C—D bonds of d_6-desmosterol in Huh7.5 cells before (*left*) and after (*right*) the hepatitis C virus (HCV) infection. The distribution of d_6-desmosterol is color-coded in *green*, while the distribution of HCV NS5A protein from immunofluorescence is color-coded in *red*. Scale bars: 10 μm [85]. (F) SRS imaging of alkynes of living *C. elegans* fed with 17-ODYA. Scale bar: 20 μm [86]. (G) SRS imaging of live neurons incubated with propargylcholine. Scale bar: 10 μm [32]. (H) SRS imaging of pancreatic cancer PANC1 cells incubated with d_7-glucose. Scale bar: 10 μm [52]. (I) The comparison of an SRS C—D image of deuterated palmitic acid (C—D SRS) and a fluorescence image of BODIPY-C_{12} (BODUPI) of COS-7 cells. Phase separation of palmitate-derived membrane domains in the ER is visualized. Overlapped signal profiles of SRS and fluorescence (on the right) show negative correlation, indicating phase separation in membrane lipids. Scale bar: 2 μm [87]. (J) SRS C—H and C—D images of melanoma M381 cells treated with d_7-glucose and SCD1 pathway inhibitor CAY before (*left two panels*) and after (*right two panels*) the detergent wash. Solid membrane domains are detected in both imaging channels. Scale bar: 20 μm [88]. (K) The DO-SRS ratiometric lipid-channel image of CD_L/CH_L of intracranial xenograft glioblastoma in mouse brain. Tumor boundary is delineated. Scale bar: 20 μm [54].

Incubating dedifferentiated melanoma cancer cells with d_7-glucose as de novo lipid synthesis tracer together with monounsaturated inhibitors, the formation of similar phase-separated solid-like ER membrane domains was also revealed (Fig. 20.4J), which are associated with the induction of apoptosis in this phenotype.

Abnormal lipid metabolism can serve as a marker for cancer cells in tumor biology. Incubated with D_2O in the growth media, tumor boundaries in mouse brain tissues were delineated with DO-SRS by ratiometric images of lipids (Fig. 20.4K) [54]. Tumor boundaries and infiltrating tumor cells in mouse xenograft of glioblastoma were also clearly identified in volumetric SRS images of C—D vibration of lipids [98]. These applications can further advance the development of stimulated Raman histology and pathology [99–101].

20.3.1.4 Glucose uptake and metabolism

Glucose is a universal energy source for all human cells. Its uptake is a major indicator of cellular energy metabolism. In addition, glucose is the major precursor for the synthesis and conversion of many downstream carbohydrates. These carbohydrates later turn into a series of energy and functional biomolecules, ranging from the energy carrier adenosine triphosphate (ATP), nicotinamide adenine dinucleotide (NADH), glycogen, nucleotides, proteins, to fatty acids [102]. These complex pathways of glucose are depicted in Fig. 20.5A. Two common glucose analogs with vibrational probes used in SRS microscopy are alkyne-tagged 3-*O*-propargyl glucose (3-OPG) and deuterated d_7-glucose. With strong Raman signals, 3-OPG has been shown to better retain the hydrophilicity of the glucose compared to its commonly used fluorescent analogs (e.g., 2-NBDG) [34, 103]. The uptake of 3-OPG was successfully visualized in neurons, brain tissues, and tumor xenograft tissues [34]. A sharp boundary of 3-OPG uptake was observed between two tumor regions (Fig. 20.5B) due to their distinct metabolic activities. However, 3-OPG cannot be phosphorylated and metabolized into downstream glucose products, thus d_7-glucose is a better choice for tracing the downstream glucose metabolism.

As summarized above in the lipid metabolism section, Li et al. reported the use of d_7-glucose to trace the de novo lipogenesis in cancer cells [52]. Additionally, Lee et al. utilized d_7-glucose to track subcellular enrichment of glycogen in a series of melanoma phenotypes (Fig. 20.5C) and showed that higher glycogen storage level leads to higher tolerance to glucose deficiency [103]. More versatile applications with deuterated glucose were achieved in the spectral tracing of deuterium (STRIDE) with SRS microscopy, allowing for the multicolor mapping of d_7-glucose-derived proteins, lipids, and DNA or glycogen in tissues after linear combination unmixing [55]. For example, lipid synthesis in the cerebellum of the mouse brain was revealed by STRIDE-SRS (Fig. 20.5D) and was correlated with the myelination process [105]. Different deuterated glucose isotopologues with distinct Raman signatures could be utilized for multicolor pulse-chase metabolic tracing [55]. Recently, Hong et al. used deuterated [3-d]-glucose and [4-d]-glucose to specifically label two NADPH production pathways—oxidative pentose phosphate pathway (oxPPP) and malic enzyme 1 (ME1)-catalyzed conversion—in adipocytes by tracing hydrides inside lipid droplets [104]. The SRS imaging results (Fig. 20.5E) suggest that NADPH from oxPPP becomes the main source when ME1-mediated NADPH production is reduced under hypoxia. In addition to using either alkyne or deuterated glucose, two-color SRS imaging for simultaneously assessing glucose uptake and metabolic conversions were also achieved by combining 3-OPG-$^{13}C_3$ and d_7-glucose in the cell culture (Fig. 20.5F and G) [57]. The ratiometric SRS images between 3-OPG-$^{13}C_3$ and d_7-glucose were found to be indicative of glucose utilization for various cell types and brain tissues.

20.3.2 SRS imaging of drug pharmacokinetics

Small drug and bio-functional molecules play important roles in mediating complex biophysical and biochemical reactions in living systems. SRS microscopy is particularly better suited to image such small molecules than fluorescence microscopy because bulkier fluorophore labels in the latter method can lead to a significant change in drug pharmacokinetics [32, 106]. Label-free SRS microscopy has proven its utility in imaging small molecules bearing distinctive Raman bands. For instance, Fu et al. have applied hyperspectral SRS microscopy to reveal intracellular concentrations of two tyrosine-kinase inhibitor (TKI) drugs of imatinib and nilotinib in living cells [106]. Both drugs were found to enrich in lysosomes (Fig. 20.6A). With cotreatment of chloroquine, the concentration of lysosome-trapped imatinib was found to be reduced, indicating the use of chloroquine may boost the drug efficacy. Furthermore, five-color SRS maps of different bands of C—C, P—O, and multiple C—H stretching of amlodipine besylate tablets from six manufacturers were examined and compared using SRS microscopy [112]. Other label-free SRS applications on drug molecules include monitoring dissolution of the hepatitis B antiviral drug entecavir embedded in a slowly releasing polymer formulation [113], mapping the plant seed coating to identify coating materials [114], imaging the distribution of chlorophyll and fungicides in plant cells and tissues [36], and quantifying dermal drug penetration and delivery [53, 115]. As an example of bio-functional

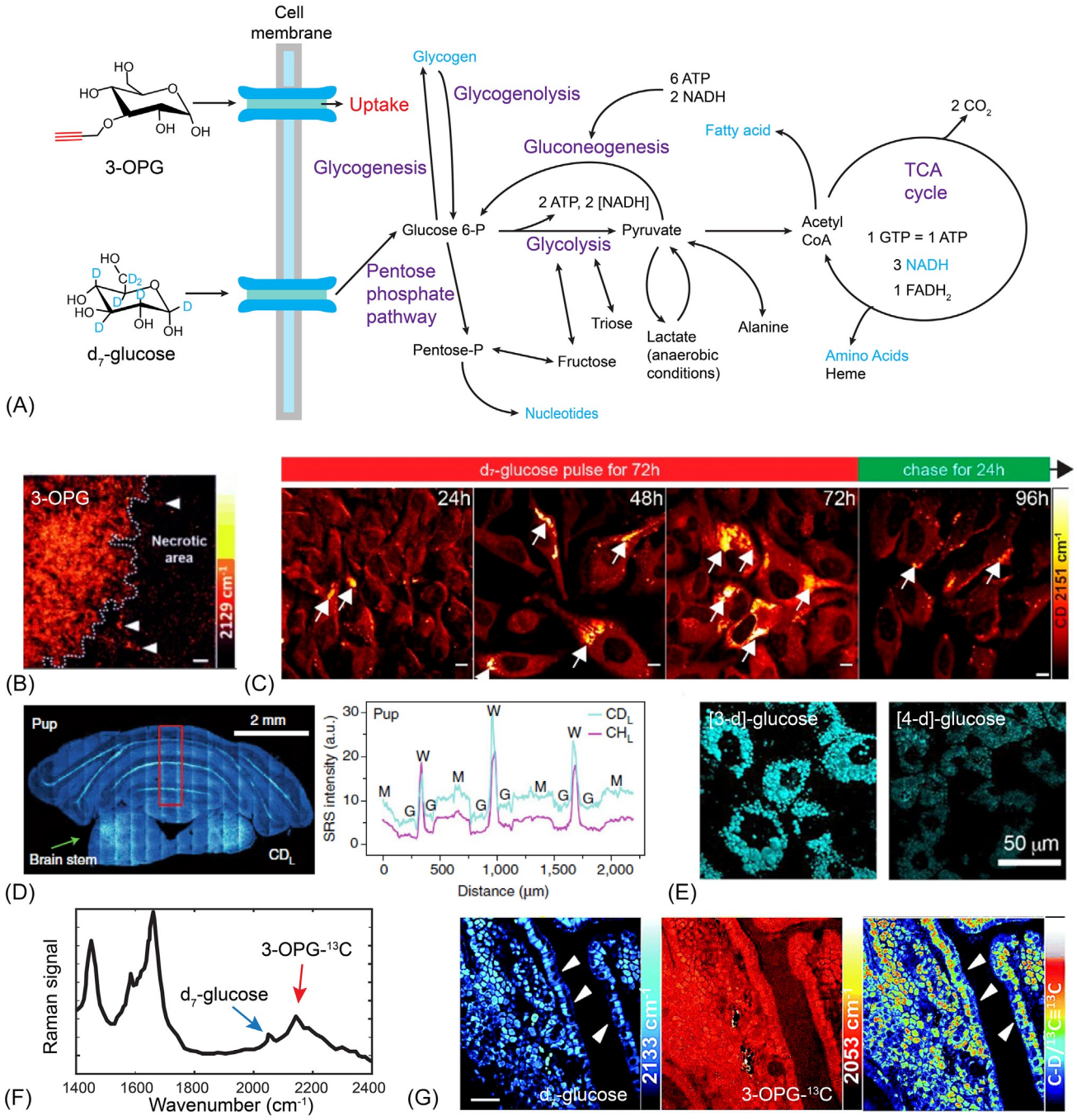

FIG. 20.5 SRS imaging of glucose metabolism. (A) Pathways *(purple)* and metabolites associated with glucose metabolism. Deuterated metabolites from d_7-glucose investigated by SRS are color-coded in *cyan*. *P*, phosphate. (B) SRS image of 3-OPG uptake in U-87 MG tumor xenograft tissues. A sharp boundary could be found between two tumor regions. Scale bar: 40 μm [34]. (C) Pulse-chase SRS imaging of glycogen in live HeLa cells by pulse treatment of d_7-glucose and chase treatment of regular glucose. Glycogen pools are indicated by *arrows*. Scale bars: 10 μm [103]. (D) STRIDE-SRS image of myelination development in pup mice fed with d_7-glucose. The *right panel* shows signal profiles of C—H and C—D obtained from the section enclosed by the *red box* in the SRS image. *M*, molecular layer; *G*, granule cell layer; *W*, white matter. Scale bar: 2 mm [55]. (E) SRS intensity ratio images of C—D/(C—D + C—H) on differentiating 3T3-L1 adipocytes treated with oxPPP pathway marker [3-*d*]-glucose (*left*) and ME1 pathway marker [4-*d*]-glucose (*right*) under hypoxia. Scale bar: 50 μm [104]. (F) Spontaneous Raman spectra of PC-3 cells cultured with d_7-glucose and then with 3-OPG-$^{13}C_3$ [57]. (G) Glucose incorporation (C—D from d_7-glucose, *left*), glucose uptake ($^{13}C{\equiv}^{13}C$ from 3-OPG-^{13}C, *middle*), and ratiometric SRS image (C—D/$^{13}C{\equiv}^{13}C$, *right*) of choroid plexus in mouse brain tissues. Scale bar: 20 μm [57].

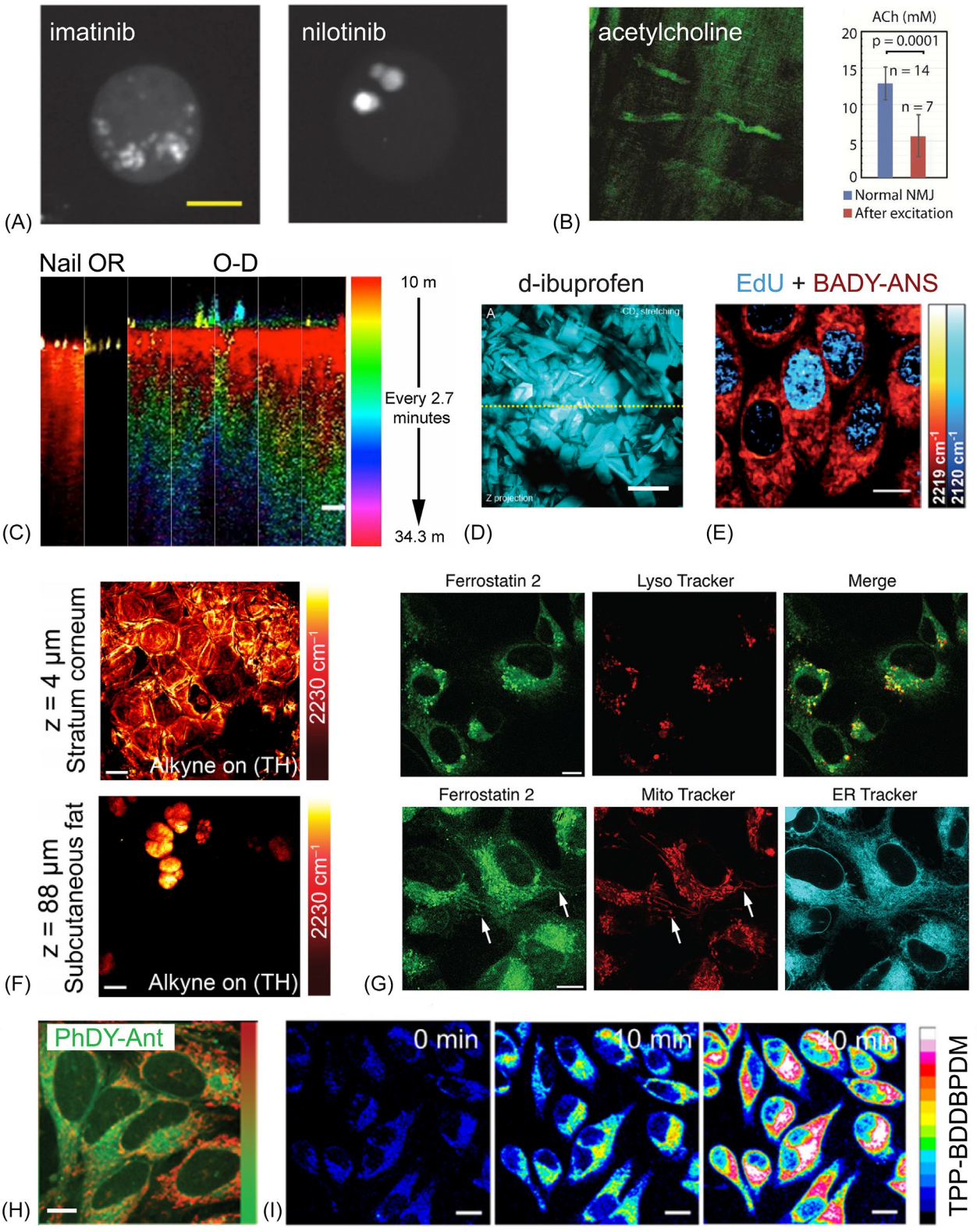

FIG. 20.6

(Continued)

molecular tracking and imaging, the concentration of the neurotransmitter acetylcholine (Ach) at the neuromuscular junction (NMJ) of frog muscle was quantified by label-free SRS imaging using the intrinsic vibration at 720 cm^{-1} of Ach [107]. The concentration of Ach was found to decrease as NMJs are excited by the electrical stimulation (Fig. 20.6B). All the above applications have demonstrated the great potential of SRS imaging in detailing the mechanism of transportation and function for drugs and other functional small molecules.

Taking a step forward, SRS microscopy with small vibrational probes has been largely used in studying many drugs and bio-functional molecules without intrinsic distinctive Raman signatures. Important drug delivery problems such as drug-solvent formulations and their effects after the application were successfully investigated with SRS microscopy. Chiu et al. used SRS microscopy to map the penetration of D_2O, deuterated propylene glycol (PG-d_8), and DMSO-d_6 into the human nail over time (Fig. 20.6C) [108]. Quick kinetics of water diffusion across the nail was revealed, which sheds light on developing new drug formulations for treating recalcitrant nail diseases. Saar et al. used SRS microscopy to image the penetration of deuterated ibuprofen into the skin surface after topical application [53]. The formation of solid ibuprofen crystals was observed (Fig. 20.6D), which was likely caused by the higher local concentration of drug molecules due to the faster penetration of the solvent PG. In another demonstration, the penetration of terbinafine hydrochloride (TH), an FDA-approved antifungal drug with an internal alkyne, was sensitively visualized by SRS microscopy after topical application to mouse ears (Fig. 20.6F) [32].

For probing drug distribution and pharmacokinetics, Gaschler et al. have used SRS microscopy to visualize the intracellular localization of alkyne-bearing ferrostatins, a group of small-molecule inhibitors of ferroptosis. Ferrostatins were found to enrich lysosomes, mitochondria, and the endoplasmic reticulum (Fig. 20.6G) [39]. In addition, cell uptake of alkyne-labeled antibiotic anisomycin (BADY-ANS) was imaged together with EdU in dual-color SRS microscopy (Fig. 20.6E) by Tipping et al., enabling the identification of intracellular drug-dependent changes [109]. Seidel et al. also utilized bioorthogonal SRS microscopy to study the structure–activity-distribution relationship of a series of alkyne-labeled anticancer antimycin-type depsipeptides (e.g., PhDY-Ant) at the single-cell level (Fig. 20.6H) [110]. Different intracellular localizations of the 15-member ring neoantimycin and the nine-member ring antimycin were revealed. Furthermore, hyperspectral SRS microscopy has also been used to track pharmacokinetics of an alkyne-labeled mitochondria-targeting molecule triphenylphosphonium (TPP) (Fig. 20.6I) [111]. Based on the better photostability of a probe molecule and linear SRS signals with low backgrounds, a quantitative model to associate the mitochondrial membrane potential with the key pharmacokinetic parameters of TPP in live cells was established.

20.3.3 Vibrational probes in chemical sensing

Besides imaging distributions and dynamic turnovers of the biological analogues, small vibrational probes can also be attached to the molecular sensor to achieve functional chemical sensing in various environments including living cells. An ideal Raman-active chemical sensor must have high specificity, strong photostability, and minimal cytotoxicity for cell samples, which should be fulfilled by the rational design [116]. A list of Raman-active chemical sensors is displayed in Section VII of Fig. 20.2. In 2018, Zeng et al. reported the first diyne-tagged Raman sensor for H_2S [62]. After reacting with H_2S, the Raman peak of the sensor molecule will be redshifted by ~10 cm^{-1} due to the end-capping substitution effect, in which H_2S cleaves azide into amine (Fig. 20.7A and B). This sensor molecule also bears a mitochondria-targeting side group, which permits subcellular chemical sensing of H_2S in mitochondria with ratiometric SRS images (Fig. 20.7C). Later,

FIG.20.6, cont'd SRS imaging of drugs and small biomolecules. (A) Maximum intensity projection of 3D SRS images of imatinib (*left*) and nilotinib (*right*), in BaF3/BCR-ABL1 cells. Scale bar: 5 μm [106]. (B) *Left*: SRS image of acetylcholine at 720 cm^{-1} in frog neuromuscular junctions (NMJs). *Right*: the concentration of acetylcholine in NMJ before and after an electrical shock, quantified by SRS spectra [107]. (C) XZ orthogonal SRS images of the penetration of D_2O into five regions in the human nail (shown as five panels on the right). The *color bar* indicates the penetration time after the D_2O application. The SRS image of keratin in the nail is shown in the first panel (Nail) and the background image is shown in the second panel (OR). The first two panels are not color-coded with time. Scale bar: 20 μm [108]. (D) SRS image of crystallized deuterated ibuprofen formed on the skin surface 25 min after the topical application with propylene glycol (PG) as the solvent. Scale bar: 50 μm [53]. (E) Merged two-color SRS image of EdU *(blue)* and BADY-ANS *(red)* in fixed SKBR3 cells. Scale bar: 10 μm [109]. (F) SRS images of terbinafine hydrochloride (TH) penetration into mouse tissue at stratum corneum and subcutaneous fat layers. Scale bars: 20 μm [32]. (G) SRS images of ferrostatin 2, an alkyne-bearing ferrostatin analog (*first column*), fluorescence images of LysoTracker and MitoTracker (*second column*), and ER Tracker (*third column*, *bottom*). A merged image of ferrostatin 2 and LysoTracker is shown in the upper panel of the third column. Scale bars: 10 μm [39]. (H) Merged image of PhDY-Ant (*green*, alkyne SRS) and mitoTracker (*red*, fluorescence) in live HeLa cells. Scale bar: 10 μm [110]. (I) SRS concentration images of real-time uptake of mitochondria targeting TPP-BDDBPDM in live HeLa cells. Concentration maps are calibrated from C≡C images at 2216 cm^{-1}. Scale bars: 10 μm [111].

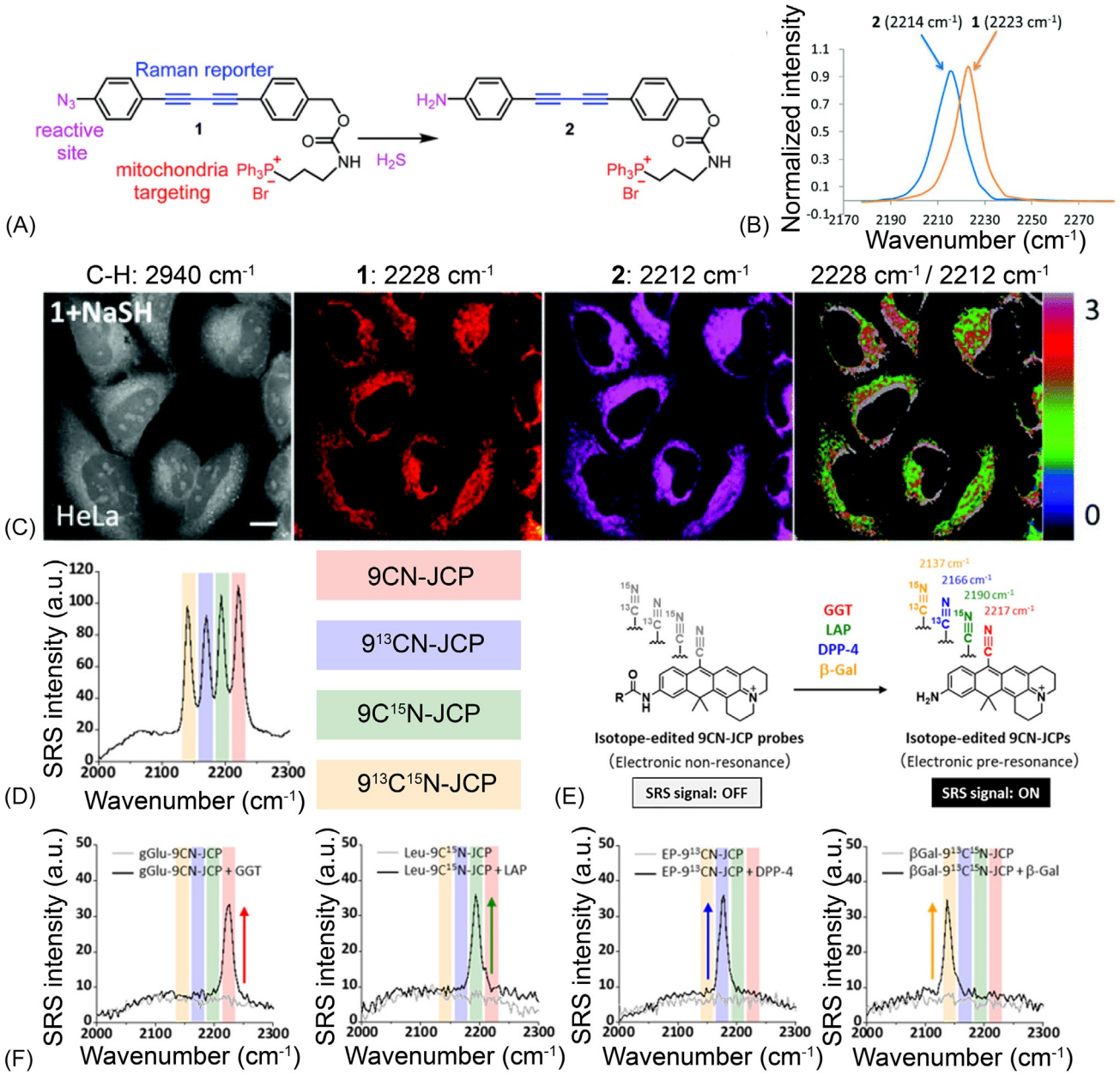

FIG. 20.7 Raman probes for chemical sensing. (A) Chemical sensing mechanism of H_2S probe **1**. After reacting with H_2S, N_3-bearing probe **1** transforms to NH_2-bearing probe **2** [62]. (B) Spontaneous Raman spectra of probe **1** and **2** in DMSO [62]. (C) SRS and ratiometric images (probe **1** intensity at $2228\,cm^{-1}$ divided by probe **2** intensity at $2212\,cm^{-1}$) of living HeLa cells. Cells are incubated with probe **1** and then NaHS. H_2S distribution in mitochondria is visualized. Scale bar 10 μm [62]. (D) SRS spectrum of a mixture of isotope-edited enzyme trackers (9CN-JCPs) in DMSO [66]. (E) Raman signal of 9CN-JCPs can be activated after reacting with enzymes [66]. (F) SRS spectra of a mixture of four 9CN-JCPs before *(gray)* and after *(black)* reacting with GGT, LAP, DPP-4, and β-Gal [66].

a group of pH-sensitive bisarylbutadiyne derivatives was developed by Wilson et al. for sensing the intracellular pH over the range from 2 to 10, based on a similar end-capping substitution effect [63]. The Raman-active pH sensors have been applied to successfully report the pH drop and recovery as a function of etoposide-induced apoptosis in prostate cancer cells. Recently, based on spontaneous Raman spectroscopy, Tipping et al. have developed 4-((trimethyl-silyl)ethynyl)benzonitrile with both alkyne and nitrile tags as the sensor for fluoride ions [64]. Also, Takemura et al. reported metal ion complexations sensors based on the phenylacetylene-tagged dipycolylaminoethyl aniline (A-DPEA), which could detect Raman band shift caused by the complexation between A-DPEA and Zn^{2+} in cells [65]. Both sensors should be applicable in SRS imaging to offer improved detection sensitivity in live cells.

Enzyme activities in living cells could also be sensed with specially tailored vibrational probes. Fujioka et al. have synthesized four types of Raman dyes (termed 9CN-JCP) with isotope-editable nitriles (Fig. 20.7D–E) [66]. Functionalized with different end groups, four dye molecules can specifically react with four enzymes: γ-glutamyl transpeptidase (GGT), leucine aminopeptidase (LAP), dipeptidyl peptidase-4 (DPP-4), and β-galactosidase (β-Gal). The linkage with enzymes in turn redshifts the absorption of dyes from visible to near-infrared, enabling the turn-on of SRS signals through electronic preresonance enhancement (Fig. 20.7F). Multicolor SRS imaging of activities of these four enzymes in living cells has been demonstrated, exhibiting cell line-dependent patterns. More details related to electronic pre-resonance will be discussed in the next chapter.

SRS spectroscopy and microscopy are also exploitable to probe the microscale distribution of temperature and solvation states. Label-free SRS imaging has been used to map microscale temperature heterogeneities based on signal ratios between the O—H band and isosbestic band at 3220 and 3420 cm^{-1}, respectively [117]. With the help of the calibration curve between the temperature and the peak ratio, the heterogeneous temperature distribution was observed within cells. In another example, using nitrile-bearing chromophore Rhodamine 800, subcellular heterogeneities of water solvation states were detected [67]. Such sensing capability relies on the vibrational Stark effect, in which changes in the solvent polarity shift the sharp Raman peak of nitriles.

20.3.4 Screening and interrogating the metabolic flux with vibrational probe sets

Instead of imaging with one or several vibrational probes for targeted metabolism, working with a set of Raman probes allows screening of the metabolic changes and integrative interrogations of metabolic flux. The use of vibrational probe sets can offer a more holistic view of metabolic status in diseased states and potentially shed light on new therapeutic strategies.

To this end, Zhang et al. screened the metabolic changes with four types of Raman vibrational probes targeting amino acids, glucose, fatty acids, and choline in MCF-7 cells undergoing epithelial-mesenchymal transition (EMT), an essential step in the cancer metabolism associated with cancer progression and metastasis [118]. Changes in anabolic metabolism during the EMT were directly visualized by SRS imaging of C—D and C≡C vibrations. As expected, anabolism of amino acids, glucose, and choline in mesenchymal cells is found to be less active than that in epithelial cells. However, although the incorporation of glucose and PA into membrane lipids becomes low, more glucose and PA were found in the lipid droplets in mesenchymal cells (Fig. 20.8A and B), indicating that mesenchymal cells can store energy in lipid droplets through lipogenesis or scavenging free fatty acids.

Similarly, the metabolic response to traumatic brain injury in mouse hippocampal slices was investigated by Hu et al. with a series of analogs to metabolites tagged with vibrational probes [74]. After the traumatic injury (Fig. 20.8C), upregulated amino acids, lipids, and choline metabolisms were observed in the hilus of the dentate gyrus (Fig. 20.8D), which is likely caused by the activation of a cascade of anabolic metabolism for cell regeneration and neuron repair. The use of multiple metabolic vibrational probes enables multiparameter Raman measurement, which can reveal convoluted metabolic response from multiple perspectives and allow for extracting rich physiological and pathological information in live cells and tissues from multidimensional results.

Moreover, Zhao et al. have used vibrational probe sets of d-AAs and d-PA in metabolic activity phenotyping (MAP) and managed to phenotype single cells based on their multidimensional metabolite Raman signals obtained with a high-throughput confocal micro-Raman spectrometer (Fig. 20.8E) [119]. Aided by principal component analysis and machine learning, they successfully identified three breast cancer subtypes and showed much better discrimination results from vibrational probe-labeled Raman than label-free Raman results (Fig. 20.8F). Although the MAP was based on spontaneous Raman spectra analysis, the same screening strategy should also work in SRS microscopy to phenotype different cells with high-throughput hyperspectral SRS imaging.

20.4 Outlook

Advancements in various technical components of SRS microscopy have been booming since its invention in 2008, allowing for the development of novel applications [8]. For fast hyperspectral SRS imaging, several multimode excitation schemes have been developed to achieve simultaneous multicolor imaging [18, 120–122]. Using broadband femtosecond lasers and ultrafast techniques, SRS images and spectra could be obtained with spectral-focusing methods [123–126], without the need to sweep the frequency stepwise of narrowband picosecond lasers. For the spatial resolution, a series of superresolution SRS techniques have been proposed to achieve the spatial resolution better than the diffraction limit [127–130]. Particularly, plasmonic enhancement brought by a sharp metallic tip can boost the spatial resolution of SRS

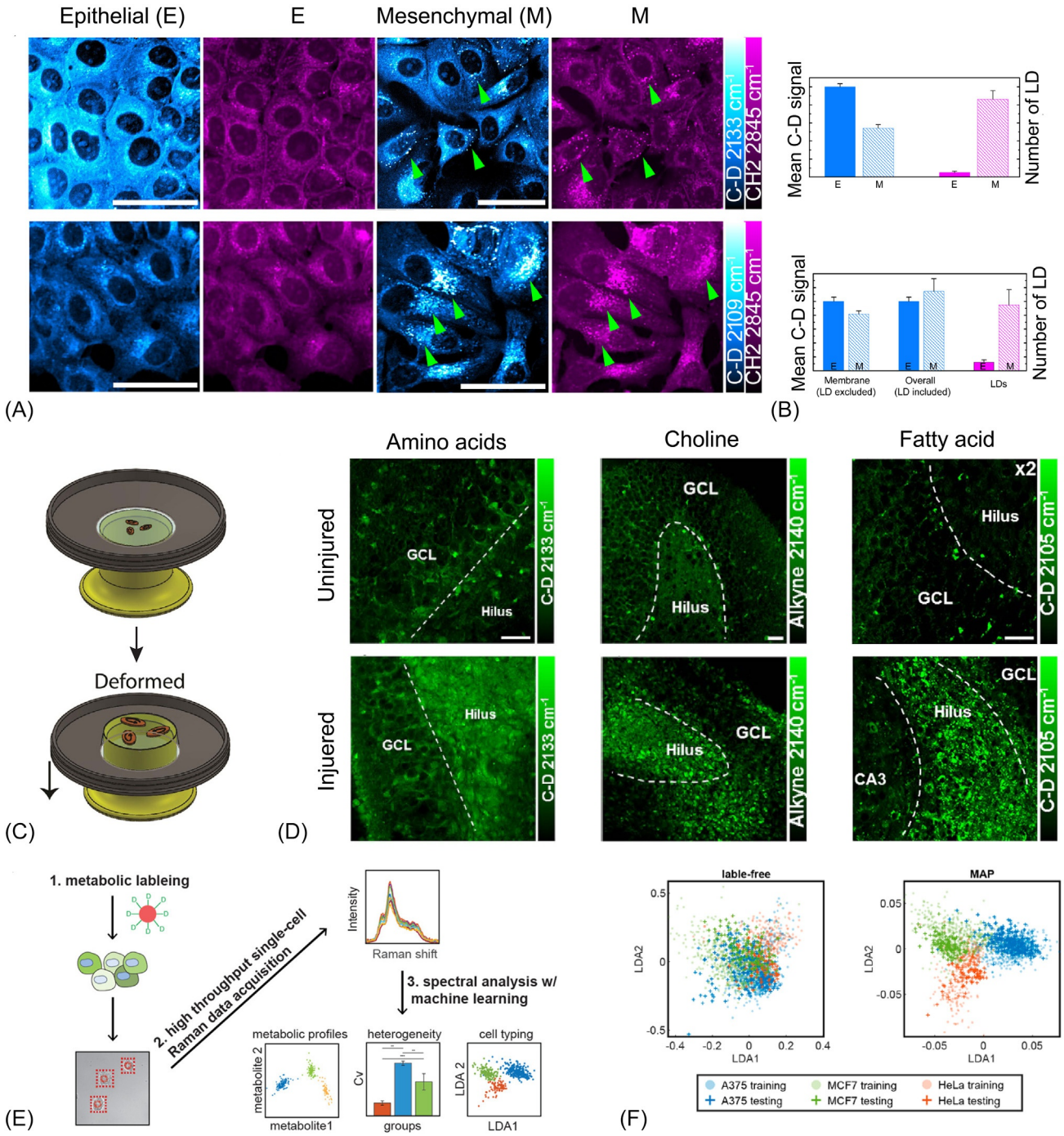

FIG. 20.8 Vibrational probe sets for screening the metabolic flux. (A) *Upper*: SRS C—D images (*blue*) and CH_2 images (*magenta*) of MCF-7 epithelial (E) and mesenchymal (M) cells incubated with d_7-glucose. *Lower*: Same C—D and CH_2 image of MCF-7 E and M cells incubated with d_{31}-palmitic acid. *Green arrows* point out bright lipid droplets. Scale bars: 50 μm [118]. (B) Bar graphs of measured C—D SRS intensity and number of lipid droplets of E and M cells obtained from (A). The upper bar graph shows glucose incorporation decreased by ~50% during EMT. The *lower bar graph* shows overall d_{31}-palmitic acid incorporation including lipid droplets is higher after EMT [118]. (C) A cartoon illustrating the device of introducing mechanical injury into slice cultures. Slice cultures are put on a silicone membrane while hollow stainless steel well is used to induce mechanical deformation [74]. (D) SRS images of amino acids, choline, and fatty acids before and after the traumatic injury. Upregulated metabolism in the hilus of the dentate gyrus is revealed for all three metabolites. Scale bars: 40 μm [74]. (E) Workflow of metabolic activity phenotyping (MAP) assisted by high-throughput confocal Raman spectroscopy of metabolic vibrational probes [119]. (F) Cell phenotyping results plotted on the linear discriminant analysis (LDA) LDA1–LDA2 plane, after dimension reduction with principal component analysis (PCA). *Left*: LDA plots with the label-free method. *Right*: LDA plots with MAP method. *Shaded dots* represent training data; *solid crosses* represent testing data. The discrimination of three cancer cell lines is achieved with MAP [119].

microscopy to reach nanoscale on material characterizations [131–133], although more efforts are still needed for demonstrations on biological samples. For the detection sensitivity, electronic preresonance SRS (epr-SRS) has been designed to advance the detection limit to the sub-μM level with 1-ms acquisition time, with chromophores absorbing light close to the SRS excitation wavelength [41, 134]. For in vivo imaging on thick tissues and living animals, epi-SRS microscopy with backward detection and a handheld epi-SRS device with fiber optics have been developed [17, 135]. For image postprocessing, a series of algorithms have been proposed, based on different principles ranging from linear unmixing [14], denoising [136], to machine learning [78, 137, 138].

Breakthroughs in technical development have driven SRS microscopy to become a versatile and robust characterization platform for a wide range of biological species in vivo. To this end, the development of vibrational probes is of high priority, as it provides crucial chemical selectivity and superb sensitivity to pinpoint molecules of interest in complex living systems, which offers the possibility of yielding new understandings for biology. To resolve complex bioprocesses in detail, the development of SRS vibrational probes could aim to encompass more small biomolecules such as neurotransmitters and cofactors. To improve the sensitivity, one could consider the electronic preresonance and develop chromophore-based vibrational probes, which can deliver not only remarkable detection sensitivity but also supermultiplex imaging capability. Toward providing comprehensive multidimensional information, better integrations of SRS information with that offered by other approaches (i.e., biochemical assays, multiomics, genome editing, etc.) could be further explored.

The specificity could also be improved in the design of vibrational probes. By introducing proper moieties into probe molecules, SRS imaging could be utilized to visualize bioactivities at subcellular targets such as organelles [43, 111]. Moreover, genetically encoded vibrational probes are needed to map in situ activities of targeted biomolecules with genetic specificity. For instance, Zhang et al. used an unnatural amino acid with Raman tags to genetically label proteins in living cells, which were then imaged by hyperspectral SRS microscopy [139]. Alternatively, genetic tools are also applicable in engineering proteins and aptamers that hold a higher affinity to vibrational probes during the incubation, thus allowing for in situ SRS imaging with high specificity.

In conclusion, the coupling of small vibrational probes with SRS imaging has become an indispensable tool in searching for new and in-depth information on complex biological processes. It is expected that the development of vibrational probes continues to grow toward higher selectivity, sensitivity, photostability, biocompatibility, and multiplexing capability. With the expanding library of novel vibrational probes for specific targets and purposes, insightful biophysical, biochemical, and biomedical discoveries will continue to unravel in the areas of cell and tissue metabolism, biomedicine, chemical sensing, disease diagnosis and treatment, and more.

References

[1] Y. Shen, F. Hu, W. Min, Raman imaging of small biomolecules, Annu. Rev. Biophys. 48 (2019) 347–369.

[2] B. Alberts, et al., Molecular Biology of the Cell, Garland Science, Taylor and Francis Group, New York, NY, 2015.

[3] N. Neave, Hormones and Behaviour: A Psychological Approach, Cambridge University Press, Cambridge, 2007.

[4] A.S. Klymchenko, R. Kreder, Fluorescent probes for lipid rafts: from model membranes to living cells, Chem. Biol. 21 (2014) 97–113.

[5] E.J. O'Rourke, A.A. Soukas, C.E. Carr, G. Ruvkun, *C. elegans* major fats are stored in vesicles distinct from lysosome-related organelles, Cell Metab. **10** (2009) 430–435.

[6] K. Yen, et al., A comparative study of fat storage quantitation in nematode Caenorhabditis elegans using label and label-free methods, PLoS One 5 (2010), e12810.

[7] E. Ploetz, S. Laimgruber, S. Berner, W. Zinth, P. Gilch, Femtosecond stimulated Raman microscopy, Appl. Phys. B 87 (2007) 389–393.

[8] C.W. Freudiger, et al., Label-free biomedical imaging with high sensitivity by stimulated Raman scattering microscopy, Science 322 (2008) 1857.

[9] P. Nandakumar, A. Kovalev, A. Volkmer, Vibrational imaging based on stimulated Raman scattering microscopy, New J. Phys. 11 (2009), 033026.

[10] Y. Ozeki, F. Dake, S.I. Kajiyama, K. Fukui, K. Itoh, Analysis and experimental assessment of the sensitivity of stimulated Raman scattering microscopy, Opt. Express **17** (2009) 3651–3658.

[11] W. Min, C.W. Freudiger, S. Lu, X.S. Xie, Coherent nonlinear optical imaging: beyond fluorescence microscopy, Annu. Rev. Phys. Chem. 62 (2011) 507–530.

[12] J.-X. Cheng, X.S. Xie, Vibrational spectroscopic imaging of living systems: an emerging platform for biology and medicine, Science **350** (2015), aaa8870.

[13] J.-X. Cheng, X.S. Xie, Coherent Raman Scattering Microscopy, CRC Press, 2016.

[14] L. Wei, et al., Imaging complex protein metabolism in live organisms by stimulated Raman scattering microscopy with isotope labeling, ACS Chem. Biol. 10 (2015) 901–908.

[15] F. Hu, L. Shi, W. Min, Biological imaging of chemical bonds by stimulated Raman scattering microscopy, Nat. Methods 16 (2019) 830–842.

[16] L. Wei, et al., Live-cell bioorthogonal chemical imaging: stimulated Raman scattering microscopy of vibrational probes, Acc. Chem. Res. 49 (2016) 1494–1502.

[17] B.G. Saar, et al., Video-rate molecular imaging in vivo with stimulated Raman scattering, Science 330 (2010) 1368.

[18] Y. Ozeki, et al., High-speed molecular spectral imaging of tissue with stimulated Raman scattering, Nat. Photonics 6 (2012) 845–851.
[19] Y. Wakisaka, et al., Probing the metabolic heterogeneity of live Euglena gracilis with stimulated Raman scattering microscopy, Nat. Microbiol. 1 (2016) 16124.
[20] M. Shamir, Y. Bar-On, R. Phillips, R. Milo, SnapShot: timescales in cell biology, Cell **164** (2016) 1302–1302.e1301.
[21] W.J. Tipping, M. Lee, A. Serrels, V.G. Brunton, A.N. Hulme, Stimulated Raman scattering microscopy: an emerging tool for drug discovery, Chem. Soc. Rev. 45 (2016) 2075–2089.
[22] H.J. Lee, J.-X. Cheng, Imaging chemistry inside living cells by stimulated Raman scattering microscopy, Methods 128 (2017) 119–128.
[23] D. Lin-Vien, N.B. Colthup, W.G. Fateley, J.G. Grasselli, The Handbook of Infrared and Raman Characteristic Frequencies of Organic Molecules, Elsevier, 1991.
[24] H. Yamakoshi, et al., Alkyne-tag Raman imaging for visualization of mobile small molecules in live cells, J. Am. Chem. Soc. 134 (2012) 20681–20689.
[25] E.M. Sletten, C.R. Bertozzi, Bioorthogonal chemistry: fishing for selectivity in a sea of functionality, Angew. Chem. Int. Ed. 48 (2009) 6974–6998.
[26] C.P. Ramil, Q. Lin, Bioorthogonal chemistry: strategies and recent developments, Chem. Commun. 49 (2013) 11007–11022.
[27] D.M. Patterson, L.A. Nazarova, J.A. Prescher, Finding the right (bioorthogonal) chemistry, ACS Chem. Biol. 9 (2014) 592–605.
[28] C.H. Camp Jr., M.T. Cicerone, Chemically sensitive bioimaging with coherent Raman scattering, Nat. Photonics 9 (2015) 295–305.
[29] Z. Zhao, Y. Shen, F. Hu, W. Min, Applications of vibrational tags in biological imaging by Raman microscopy, Analyst 142 (2017) 4018–4029.
[30] H. Yamakoshi, et al., Imaging of EdU, an alkyne-tagged cell proliferation probe, by Raman microscopy, J. Am. Chem. Soc. 133 (2011) 6102–6105.
[31] L. Lin, et al., A bioorthogonal Raman reporter strategy for SERS detection of Glycans on live cells, Angew. Chem. Int. Ed. 52 (2013) 7266–7271.
[32] L. Wei, et al., Live-cell imaging of alkyne-tagged small biomolecules by stimulated Raman scattering, Nat. Methods 11 (2014) 410–412.
[33] S. Hong, et al., Live-cell stimulated Raman scattering imaging of alkyne-tagged biomolecules, Angew. Chem. Int. Ed. 53 (2014) 5827–5831.
[34] F. Hu, et al., Vibrational imaging of glucose uptake activity in live cells and tissues by stimulated Raman scattering, Angew. Chem. Int. Ed. 54 (2015) 9821–9825.
[35] Z. Chen, et al., Multicolor live-cell chemical imaging by isotopically edited alkyne vibrational palette, J. Am. Chem. Soc. 136 (2014) 8027–8033.
[36] J.C. Mansfield, et al., Label-free chemically specific imaging in planta with stimulated Raman scattering microscopy, Anal. Chem. 85 (2013) 5055–5063.
[37] J.M. Crawford, C. Portmann, X. Zhang, M.B.J. Roeffaers, J. Clardy, Small molecule perimeter defense in entomopathogenic bacteria, Proc. Natl. Acad. Sci. 109 (2012) 10821.
[38] H.J. Lee, et al., Assessing cholesterol storage in live cells and *C. elegans* by stimulated Raman scattering imaging of phenyl-diyne cholesterol, Sci. Report. **5** (2015) 7930.
[39] M.M. Gaschler, et al., Determination of the subcellular localization and mechanism of action of Ferrostatins in suppressing Ferroptosis, ACS Chem. Biol. 13 (2018) 1013–1020.
[40] J.Y. Lee, S.B. Suh, K.S. Kim, Polyenes vs polyynes: efficient π-frame for nonlinear optical pathways, J. Chem. Phys. 112 (1999) 344–348.
[41] L. Wei, et al., Super-multiplex vibrational imaging, Nature 544 (2017) 465–470.
[42] F. Hu, et al., Supermultiplexed optical imaging and barcoding with engineered polyynes, Nat. Methods 15 (2018) 194–200.
[43] S. Tian, et al., Polydiacetylene-based ultrastrong bioorthogonal Raman probes for targeted live-cell Raman imaging, Nat. Commun. 11 (2020) 81.
[44] J.C.M. van Hest, K.L. Kiick, D.A. Tirrell, Efficient incorporation of unsaturated methionine analogues into proteins in vivo, J. Am. Chem. Soc. 122 (2000) 1282–1288.
[45] K.E. Beatty, et al., Fluorescence visualization of newly synthesized proteins in mammalian cells, Angew. Chem. Int. Ed. 45 (2006) 7364–7367.
[46] R. Milo, What is the total number of protein molecules per cell volume? A call to rethink some published values, BioEssays 35 (2013) 1050–1055.
[47] F.H. Crick, Symposia of the Society for Experimental Biology, vol. 12, 1958, p. 8.
[48] L. Wei, Y. Yu, Y. Shen, M.C. Wang, W. Min, Vibrational imaging of newly synthesized proteins in live cells by stimulated Raman scattering microscopy, Proc. Natl. Acad. Sci. 110 (2013) 11226.
[49] F. Hu, L. Wei, C. Zheng, Y. Shen, W. Min, Live-cell vibrational imaging of choline metabolites by stimulated Raman scattering coupled with isotope-based metabolic labeling, Analyst 139 (2014) 2312–2317.
[50] D. Zhang, M.N. Slipchenko, J.-X. Cheng, Highly sensitive vibrational imaging by femtosecond pulse stimulated Raman loss, J. Phys. Chem. Lett. 2 (2011) 1248–1253.
[51] G. Alba Alfonso, G.P. Simon, R. Howard, I. Elina, O.P. Eric, D38-cholesterol as a Raman active probe for imaging intracellular cholesterol storage, J. Biomed. Opt. 21 (2015) 1–8.
[52] J. Li, J.-X. Cheng, Direct visualization of De novo lipogenesis in single living cells, Sci. Rep. 4 (2014) 6807.
[53] B.G. Saar, L.R. Contreras-Rojas, X.S. Xie, R.H. Guy, Imaging drug delivery to skin with stimulated Raman scattering microscopy, Mol. Pharm. 8 (2011) 969–975.
[54] L. Shi, et al., Optical imaging of metabolic dynamics in animals, Nat. Commun. 9 (2018) 2995.
[55] L. Zhang, et al., Spectral tracing of deuterium for imaging glucose metabolism, Nat. Biomed. Eng. 3 (2019) 402–413.
[56] Y. Shen, F. Xu, L. Wei, F. Hu, W. Min, Live-cell quantitative imaging of proteome degradation by stimulated Raman scattering, Angew. Chem. Int. Ed. 53 (2014) 5596–5599.
[57] R. Long, et al., Two-color vibrational imaging of glucose metabolism using stimulated Raman scattering, Chem. Commun. 54 (2018) 152–155.
[58] Q. Jin, et al., Multicolor Raman beads for multiplexed tumor cell and tissue imaging and in vivo tumor spectral detection, Anal. Chem. 91 (2019) 3784–3789.

[59] S. Vanden-Hehir, et al., Alkyne-tagged PLGA allows direct visualization of nanoparticles in vitro and ex vivo by stimulated Raman scattering microscopy, Biomacromolecules 20 (2019) 4008–4014.
[60] S. Vanden-Hehir, et al., Raman imaging of nanocarriers for drug delivery, Nanomaterials 9 (2019) 341.
[61] F. Hu, S.D. Brucks, T.H. Lambert, L.M. Campos, W. Min, Stimulated Raman scattering of polymer nanoparticles for multiplexed live-cell imaging, Chem. Commun. 53 (2017) 6187–6190.
[62] C. Zeng, F. Hu, R. Long, W. Min, A ratiometric Raman probe for live-cell imaging of hydrogen sulfide in mitochondria by stimulated Raman scattering, Analyst 143 (2018) 4844–4848.
[63] L.T. Wilson, et al., A new class of ratiometric small molecule intracellular pH sensors for Raman microscopy, Analyst 145 (2020) 5289–5298.
[64] W.J. Tipping, et al., Ratiometric sensing of fluoride ions using Raman spectroscopy, Chem. Commun. 56 (2020) 14463–14466.
[65] S. Takemura, H. Watanabe, T. Nishihara, A. Okamoto, K. Tanabe, Monitoring intracellular metal ion complexation with an acetylene-tagged ligand by Raman spectroscopy, RSC Adv. 10 (2020) 36119–36123.
[66] H. Fujioka, et al., Multicolor activatable Raman probes for simultaneous detection of plural enzyme activities, J. Am. Chem. Soc. 142 (2020) 20701–20707.
[67] X. Lang, K. Welsher, Mapping solvation heterogeneity in live cells by hyperspectral stimulated Raman scattering microscopy, J. Chem. Phys. 152 (2020) 174201.
[68] M. Grammel, H.C. Hang, Chemical reporters for biological discovery, Nat. Chem. Biol. 9 (2013) 475–484.
[69] F. Otto, K.C. Tsou, A comparative study of DAPI, DIPI, and Hoechst 33258 and 33342 as chromosomal DNA stains, Stain Technol. 60 (1985) 7–11.
[70] F. Dolbeare, H. Gratzner, M.G. Pallavicini, J.W. Gray, Flow cytometric measurement of total DNA content and incorporated bromodeoxyuridine, Proc. Natl. Acad. Sci. 80 (1983) 5573.
[71] A. Salic, T.J. Mitchison, A chemical method for fast and sensitive detection of DNA synthesis in vivo, Proc. Natl. Acad. Sci. 105 (2008) 2415.
[72] D.C. Kennedy, et al., Cellular consequences of copper complexes used to catalyze bioorthogonal click reactions, J. Am. Chem. Soc. 133 (2011) 17993–18001.
[73] F.-K. Lu, et al., Label-free DNA imaging in vivo with stimulated Raman scattering microscopy, Proc. Natl. Acad. Sci. 112 (2015) 11624.
[74] F. Hu, M.R. Lamprecht, L. Wei, B. Morrison, W. Min, Bioorthogonal chemical imaging of metabolic activities in live mammalian hippocampal tissues with stimulated Raman scattering, Sci. Rep. 6 (2016) 39660.
[75] K. Miao, L. Wei, Live-cell imaging and quantification of PolyQ aggregates by stimulated Raman scattering of selective deuterium labeling, ACS Cent. Sci. 6 (2020) 478–486.
[76] M. Ji, et al., Rapid, label-free detection of brain tumors with stimulated raman scattering microscopy, Sci. Transl. Med. **5** (2013), 201ra119.
[77] M. Ji, et al., Detection of human brain tumor infiltration with quantitative stimulated Raman scattering microscopy, Sci. Transl. Med. **7** (2015), 309ra163.
[78] D.A. Orringer, et al., Rapid intraoperative histology of unprocessed surgical specimens via fibre-laser-based stimulated Raman scattering microscopy, Nat. Biomed. Eng. 1 (2017) 0027.
[79] M. Ji, et al., Label-free imaging of amyloid plaques in Alzheimer's disease with stimulated Raman scattering microscopy, Sci. Adv. **4** (2018), eaat7715.
[80] E.R. Kandel, The molecular biology of memory storage: a dialogue between genes and synapses, Science 294 (2001) 1030.
[81] D.-e. Sun, X. Chen, Raman imaging shines a light on neurodegenerative disorders, ACS Cent. Sci. 6 (2020) 459–460.
[82] D. Fu, et al., In vivo metabolic fingerprinting of neutral lipids with hyperspectral stimulated Raman scattering microscopy, J. Am. Chem. Soc. 136 (2014) 8820–8828.
[83] J. Li, et al., Lipid desaturation is a metabolic marker and therapeutic target of ovarian cancer stem cells, Cell Stem Cell **20** (2017) 303–314.e305.
[84] J. Garcia-Bermudez, et al., Squalene accumulation in cholesterol auxotrophic lymphomas prevents oxidative cell death, Nature 567 (2019) 118–122.
[85] V.A. Villareal, D. Fu, D.A. Costello, X.S. Xie, P.L. Yang, Hepatitis C virus selectively alters the intracellular localization of desmosterol, ACS Chem. Biol. 11 (2016) 1827–1833.
[86] X. Li, et al., Quantitative imaging of lipid synthesis and lipolysis dynamics in Caenorhabditis elegans by stimulated Raman scattering microscopy, Anal. Chem. 91 (2019) 2279–2287.
[87] Y. Shen, et al., Metabolic activity induces membrane phase separation in endoplasmic reticulum, Proc. Natl. Acad. Sci. 114 (2017) 13394.
[88] J. Du, et al., Raman-guided subcellular pharmaco-metabolomics for metastatic melanoma cells, Nat. Commun. 11 (2020) 4830.
[89] Z. Movasaghi, S. Rehman, I.U. Rehman, Raman spectroscopy of biological tissues, Appl. Spectrosc. Rev. 42 (2007) 493–541.
[90] J.L. Suhalim, et al., Characterization of cholesterol crystals in atherosclerotic plaques using stimulated Raman scattering and second-harmonic generation microscopy, Biophys. J. 102 (2012) 1988–1995.
[91] P. Wang, et al., Label-free quantitative imaging of cholesterol in intact tissues by hyperspectral stimulated Raman scattering microscopy, Angew. Chem. Int. Ed. 52 (2013) 13042–13046.
[92] F. Tian, et al., Monitoring peripheral nerve degeneration in ALS by label-free stimulated Raman scattering imaging, Nat. Commun. 7 (2016) 13283.
[93] G.S. Abela, et al., Effect of cholesterol crystals on plaques and intima in arteries of patients with acute coronary and cerebrovascular syndromes, Am. J. Cardiol. 103 (2009) 959–968.
[94] P. Duewell, et al., NLRP3 inflammasomes are required for atherogenesis and activated by cholesterol crystals, Nature 464 (2010) 1357–1361.
[95] S. Yue, et al., Cholesteryl ester accumulation induced by PTEN loss and PI3K/AKT activation underlies human prostate cancer aggressiveness, Cell Metab. 19 (2014) 393–406.
[96] Y. Yu, A.S. Mutlu, H. Liu, M.C. Wang, High-throughput screens using photo-highlighting discover BMP signaling in mitochondrial lipid oxidation, Nat. Commun. 8 (2017) 865.

[97] S.H. Zeisel, J.K. Blusztajn, Choline and human nutrition, Annu. Rev. Nutr. 14 (1994) 269–296.
[98] M. Wei, et al., Volumetric chemical imaging by clearing-enhanced stimulated Raman scattering microscopy, Proc. Natl. Acad. Sci. 116 (2019) 6608.
[99] F.-K. Lu, et al., Label-free neurosurgical pathology with stimulated Raman imaging, Cancer Res. 76 (2016) 3451.
[100] L. Zhang, et al., Rapid histology of laryngeal squamous cell carcinoma with deep-learning based stimulated Raman scattering microscopy, Theranostics 9 (2019) 2541–2554.
[101] T.C. Hollon, et al., Near real-time intraoperative brain tumor diagnosis using stimulated Raman histology and deep neural networks, Nat. Med. 26 (2020) 52–58.
[102] R.J. Shaw, Glucose metabolism and cancer, Curr. Opin. Cell Biol. 18 (2006) 598–608.
[103] D. Lee, et al., Visualizing subcellular enrichment of glycogen in live cancer cells by stimulated Raman scattering, Anal. Chem. 92 (2020) 13182–13191.
[104] S. Hong, et al., Live-cell imaging of NADPH production from specific pathways, CCS Chemistry 3 (2020) 1642–1648.
[105] H. Jurevics, P. Morell, Cholesterol for synthesis of myelin is made locally, Not Imported into Brain, J. Neurochem. 64 (1995) 895–901.
[106] D. Fu, et al., Imaging the intracellular distribution of tyrosine kinase inhibitors in living cells with quantitative hyperspectral stimulated Raman scattering, Nat. Chem. 6 (2014) 614–622.
[107] D. Fu, W. Yang, X.S. Xie, Label-free imaging of neurotransmitter acetylcholine at neuromuscular junctions with stimulated Raman scattering, J. Am. Chem. Soc. 139 (2017) 583–586.
[108] W.S. Chiu, et al., Molecular diffusion in the human nail measured by stimulated Raman scattering microscopy, Proc. Natl. Acad. Sci. 112 (2015) 7725.
[109] W.J. Tipping, M. Lee, A. Serrels, V.G. Brunton, A.N. Hulme, Imaging drug uptake by bioorthogonal stimulated Raman scattering microscopy, Chem. Sci. 8 (2017) 5606–5615.
[110] J. Seidel, et al., Structure–activity–distribution relationship study of anti-cancer antimycin-type depsipeptides, Chem. Commun. 55 (2019) 9379–9382.
[111] K. Bae, W. Zheng, Y. Ma, Z. Huang, Real-time monitoring of pharmacokinetics of mitochondria-targeting molecules in live cells with bioorthogonal hyperspectral stimulated Raman scattering microscopy, Anal. Chem. 92 (2020) 740–748.
[112] M.N. Slipchenko, et al., Vibrational imaging of tablets by epi-detected stimulated Raman scattering microscopy, Analyst 135 (2010) 2613–2619.
[113] A.T. Francis, et al., In situ stimulated Raman scattering (SRS) microscopy study of the dissolution of sustained-release implant formulation, Mol. Pharm. 15 (2018) 5793–5801.
[114] C.-C. Wang, et al., In situ chemically specific mapping of agrochemical seed coatings using stimulated Raman scattering microscopy, J. Biophotonics 11 (2018), e201800108.
[115] C.-S. Liao, et al., Spectrometer-free vibrational imaging by retrieving stimulated Raman signal from highly scattered photons, Sci. Adv. 1 (2015), e1500738.
[116] W. Goepel, T.A. Jones, M. Kleitz, I. Lundström, T. Seiyama, Sensors, Chemical and Biochemical Sensors, vol. 2, John Wiley & Sons, 2008.
[117] B. Figueroa, R. Hu, S.G. Rayner, Y. Zheng, D. Fu, Real-time microscale temperature imaging by stimulated Raman scattering, J. Phys. Chem. Lett. 11 (2020) 7083–7089.
[118] Z. Luyuan, M. Wei, Bioorthogonal chemical imaging of metabolic changes during epithelial–mesenchymal transition of cancer cells by stimulated Raman scattering microscopy, J. Biomed. Opt. 22 (2017) 1–7.
[119] Z. Zhao, C. Chen, H. Xiong, J. Ji, W. Min, Metabolic activity phenotyping of single cells with multiplexed vibrational probes, Anal. Chem. 92 (2020) 9603–9612.
[120] C.-S. Liao, et al., Microsecond scale vibrational spectroscopic imaging by multiplex stimulated Raman scattering microscopy, Light Sci. Appl. 4 (2015) e265.
[121] W. Yang, A. Li, Y. Suo, F.-K. Lu, X. Sunney Xie, Simultaneous two-color stimulated Raman scattering microscopy by adding a fiber amplifier to a 2 ps OPO-based SRS microscope, Opt. Lett. 42 (2017) 523–526.
[122] Y. Suzuki, et al., Label-free chemical imaging flow cytometry by high-speed multicolor stimulated Raman scattering, Proc. Natl. Acad. Sci. 116 (2019) 15842.
[123] E.R. Andresen, P. Berto, H. Rigneault, Stimulated Raman scattering microscopy by spectral focusing and fiber-generated soliton as stokes pulse, Opt. Lett. 36 (2011) 2387–2389.
[124] D. Fu, G. Holtom, C. Freudiger, X. Zhang, X.S. Xie, Hyperspectral imaging with stimulated Raman scattering by chirped femtosecond lasers, J. Phys. Chem. B 117 (2013) 4634–4640.
[125] R. He, et al., Stimulated Raman scattering microscopy and spectroscopy with a rapid scanning optical delay line, Opt. Lett. 42 (2017) 659–662.
[126] M.S. Alshaykh, et al., High-speed stimulated hyperspectral Raman imaging using rapid acousto-optic delay lines, Opt. Lett. 42 (2017) 1548–1551.
[127] L. Gong, H. Wang, Breaking the diffraction limit by saturation in stimulated-Raman-scattering microscopy: a theoretical study, Phys. Rev. A 90 (2014), 013818.
[128] L. Gong, H. Wang, Suppression of stimulated Raman scattering by an electromagnetically-induced-transparency—like scheme and its application for super-resolution microscopy, Phys. Rev. A 92 (2015), 023828.
[129] D. Kim, et al., Selective suppression of stimulated Raman scattering with another competing stimulated Raman scattering, J. Phys. Chem. Lett. 8 (2017) 6118–6123.
[130] L. Gong, W. Zheng, Y. Ma, Z. Huang, Saturated stimulated-Raman-scattering microscopy for far-field superresolution vibrational imaging, Phys. Rev. Appl. 11 (2019), 034041.

[131] I. Rajapaksa, H. Kumar Wickramasinghe, Raman spectroscopy and microscopy based on mechanical force detection, Appl. Phys. Lett. 99 (2011) 161103.
[132] R.C. Prince, R.R. Frontiera, E.O. Potma, Stimulated Raman scattering: from bulk to nano, Chem. Rev. 117 (2017) 5070–5094.
[133] L.M.B.V.A. Tamma, J.S. Shumaker-Parry, H.K. Wickramasinghe, Detecting stimulated Raman responses of molecules in plasmonic gap using photon induced forces, Opt. Express **26** (2018) 31439–31453.
[134] L. Wei, W. Min, Electronic preresonance stimulated Raman scattering microscopy, J. Phys. Chem. Lett. 9 (2018) 4294–4301.
[135] C.-S. Liao, et al., In vivo and in situ spectroscopic imaging by a handheld stimulated Raman scattering microscope, ACS Photonics 5 (2018) 947–954.
[136] C.-S. Liao, J.H. Choi, D. Zhang, S.H. Chan, J.-X. Cheng, Denoising stimulated Raman spectroscopic images by total variation minimization, J. Phys. Chem. C 119 (2015) 19397–19403.
[137] A. Alfonso-García, et al., A machine learning framework to analyze hyperspectral stimulated Raman scattering microscopy images of expressed human meibum, J. Raman Spectrosc. 48 (2017) 803–812.
[138] J. Zhang, J. Zhao, H. Lin, Y. Tan, J.-X. Cheng, High-speed chemical imaging by dense-net learning of femtosecond stimulated Raman scattering, J. Phys. Chem. Lett. 11 (2020) 8573–8578.
[139] J. Zhang, et al., Small unnatural amino acid carried Raman tag for molecular imaging of genetically targeted proteins, J. Phys. Chem. Lett. 9 (2018) 4679–4685.